T.R.

GEBZE TECHNICAL UNIVERSITY

GRADUATE SCHOOL OF NATURAL AND APPLIED SCIENCES

THE USE OF ATOMIC SENSOR FOR MEASUREMENTS OF HIGH LEVEL ELECTROMAGNETIC WAVES

ÇAĞLAR ASLAN

A THESIS SUBMITTED FOR THE DEGREE OF

MASTER OF SCIENCE

DEPARTMENT OF PHYSICS

METROLOGY PROGRAMME

GEBZE

2019

T.R.

GEBZE TECHNICAL UNIVERSITY

GRADUATE SCHOOL OF NATURAL AND APPLIED SCIENCES

THE USE OF ATOMIC SENSOR FOR MEASUREMENT OF HIGH LEVEL ELECTROMAGNETIC WAVES

ÇAĞLAR ASLAN

A THESIS SUBMITTED FOR THE DEGREE OF

MASTER OF SCIENCE

DEPARTMENT OF PHYSICS

METROLOGY PROGRAMME

THESIS SUPERVISOR

PROF. DR. SAVAŞ BERBER

II. THESIS SUPERVISOR

DR. MUSTAFA ÇETİNTAŞ

GEBZE

2019

T.C.
GEBZE TEKNİK ÜNİVERSİTESİ
FEN BİLİMLERİ ENSTİTÜSÜ

YÜKSEK SEVİYELİ ELEKTROMANYETİK DALGALARIN ÖLÇÜMLERİ İÇİN ATOMİK SENSÖRÜN KULLANIMI

ÇAĞLAR ASLAN
YÜKSEK LİSANS TEZİ
FİZİK ANABİLİM DALI
METROLOJİ PROGRAMI

DANIŞMANI
PROF. DR. SAVAŞ BERBER
II. DANIŞMANI
DR. MUSTAFA ÇETİNTAŞ

GEBZE
2019

GEBZE TEKNİK ÜNİVERSİTESİ	YÜKSEK LİSANS JÜRİ ONAY FORMU

GTÜ Fen Bilimleri Enstitüsü Yönetim Kurulu'nun 12/06/2019 tarih ve 2019/26 sayılı kararıyla oluşturulan jüri tarafından 14/06/2019 tarihinde tez savunma sınavı yapılan Çağlar Aslan'ın tez çalışması Fizik Anabilim Dalı Metroloji Programında YÜKSEK LİSANS tezi olarak kabul edilmiştir.

JÜRİ

ÜYE (TEZ DANIŞMANI)	: Prof. Dr. Savaş BERBER
ÜYE	: Prof. Dr. F. Necati ECEVİT
ÜYE	: Prof. Dr. İsmail H. TAYYAR

ONAY

Gebze Teknik Üniversitesi Fen Bilimleri Enstitüsü Yönetim Kurulu'nun

...../...../..... tarih ve ...../..... sayılı kararı.

SUMMARY

In this study it has been worked, for the first time to experimentally verify the theoretical electrical field strength value of the reverberation chambers used for EMC/EMI tests and scientific studies at high levels of electromagnetic field, which cannot be verified experimentally but only calculated based on the statistical methods, by using a Cs atomic sensor based on the laser - atom - microwave interaction. Firstly, $6S_{1/2}$ (F=3) ↔ $6P_{3/2}$ (F=3, 4, 5) energy transitions of Cs atomic sensor were scanned during D_2 line by using laser light and the laser frequency was locked on the $6S_{1/2}$ (F=4) ↔ $6P_{3/2}$ (F=4) energy transition among the transitions. After this stage, the DROR resonance was observed with the applying microwave field at 9,192 GHz frequency that corresponds to $6S_{1/2}$ (F=3) ↔ $6S_{1/2}$ (F=4) energy transition and the Zeeman splits of DROR resonance was observed under the DC magnetic field. The band width and amplitude measurement changes depending on the high level electromagnetic field applying with the horn antenna was investigated between 500 V/m and 7.5 kV/m within the anechoic chamber, of Zeeman resonance of $6S_{1/2}$ (F=3, m_F=0) ↔ $6S_{1/2}$ (F=4, m_F= 0) π- transition, which is going to be used to find the dynamic operation range of the atomic sensor. Afterwards the atomic sensor was placed within the reverberation chamber and the changes of the resonances within the reverberation chamber obtained from the atomic transitions, which are completely homogeneous and direction-independent, were investigated under the microwave field. Based on the experimental data obtained from the measurements, it has been discussed to use atomic sensors to sensing high level electromagnetic fields and to verify the high level microwave fields generated within reverberation chambers.

Key Words: Reverberation chambers, laser-atom-microwave interaction, atomic sensors.

ÖZET

Bu çalışmada ilk defa EMC/EMI testlerinde ve bilimsel çalışmalarda kullanılan çınlama odalarının yüksek elektromanyetik alan seviyelerinde deneysel olarak doğrulanamayan ve ancak istatistiksel yöntemlere dayalı olarak hesaplanabilen teorik elektrik alan değerinin lazer-atom-mikrodalga etkileşimine dayanan bir Cs atomik sensor kullanılarak deneysel olarak doğrulanması çalışılmıştır. İlk olarak çalışmada lazer ışını ile Cs atomik sensörünün D_2 geçişinde $6S_{1/2}$ (F=3) ↔ $6P_{3/2}$ (F=3, 4, 5) enerji geçişleri taranmış, lazerin ışınının frekansı bu geçişlerden $6S_{1/2}$ (F=4) ↔ $6P_{3/2}$ (F=4) enerji geçişine kilitlenmiştir. Bu aşamadan sonra $6S_{1/2}$ (F=3)↔ $6S_{1/2}$ (F=4) enerji geçişine denk gelen 9,192 GHz frekansında mikrodalga alan ile DROR rezonansı gözlenmiş ve DC manyetik alan altında DROR rezonansının Zeeman ayrışması üretilmiştir. Atomik sensörün dinamik çalışma aralığını bulmak için kullanılacak olan $6S_{1/2}$ (F=3, m_F=0) ↔ $6S_{1/2}$ (F=4, m_F= 0) π-geçişinin Zeeman rezonansının ekranlı oda içinde 500 V/m ile 7.5 kV/m arasında horn anten ile uygulanan yüksek seviyeli elektromanyetik alana bağlı olarak bant genişliği ve genlik ölçümlerinin değişimi araştırılmıştır. Daha sonra atomik sensör çınlama odası içerisine yerleştirilmiş, atomik geçişlerden elde edilen rezonansların çınlama odası içinde oluşturulan tümüyle homojen ve yönden bağımsız mikrodalga alan altındaki değişimleri incelenmiştir. Ölçümlerden elde edilen deneysel verilere dayanarak atomik sensörlerin yüksek seviyeli elektromanyetik alanların algılanmasında ve çınlama odaları içerisinde oluşturulan yüksek seviyeli mikrodalga alanların doğrulanmasında bir yöntem olarak kullanılması tartışılmıştır.

Anahtar Kelimeler: Çınlama odaları, lazer-atom-mikrodalga etkileşimi, atomic sensörler.

ACKNOWLEDGEMENTS

I would like to thank and present my deepest regards to my first supervisor, Prof. Dr. Savaş BERBER for his theoretical and practical support in addition to his motivational guidance.

I would like to express my deepest and sincere regards to my second supervisor responsible of UME (National Metrology Institute) Dr. Mustafa ÇETİNTAŞ for his technical, theoretical and experimental support. His support and encouragement gave me a chance to perform this work.

I wish to express my warm and sincere thanks to Assoc. Prof. Dr. Ramiz Hamid to share his profound scientific knowledge with me.

I want to thank to my colleagues in UME Electromagnetic Laboratory personnels at first Dr. Soydan ÇAKIR and Osman ŞEN for they shared with me their experiences and software supports, Savaş ACAK for the beneficial discussions and technical support to this work. Also, I want to thank to Time and Frequency Laboratory personnels at first Dr. Ersoy ŞAHİN for his helpful discussions and the support in using some of the devices and optical apparatuses used in the study.

Finally, I am grateful to my parents for their infinitive support, my wife for her love and her magic touch to my life.

TABLE of CONTENTS

LIST of ABBREVIATIONS and ACRONYMS

Abbreviations and Acronyms		**Explanations**
Δ	:	Laplace operator
∇	:	Divergence operator
λ	:	Wave length, (m)
Ω	:	Impedance, (ohm)
τ		Life time
%	:	Percentage
η_0	:	Free space impedance, (ohm)
μm	:	Micro meter
μs	:	Micro second
μV	:	Micro Volt
M	:	Atomic mass
m_e	:	Electron mass, (kg)
Rb	:	Rubidium
Cs	:	Cesium
c	:	Speed of light, (m/s)
D	:	Dimension, (m)
d	:	Distance, (m)
D_2	:	Transition between $6S_{1/2}$ and $6P_{3/2}$ of Cesium atom
e	:	Elementary charge, (coulombs)
E_x	:	Electric field component at x-direction in cartesian coordinate system
E_y	:	Electric field component at y-direction in cartesian coordinate system
E_z	:	Electric field component at z-direction in cartesian coordinate system
E_n	:	Energy levels, (eV)
H	:	Magnetic field, (A/m)
Vp-p	:	Peak to peak amplitude voltage, (V)

au	:	Arbitrary unit
BNC	:	Bayonet Neill Concelman
cm	:	Centimeter
CW	:	Continuous Wave
dB	:	Decibel
dBm	:	Decibel mili watt
DC	:	Direct current
div	:	Division
DUT		Device Under Test
eV	:	Electron Volt
EM	:	Electromagnetic
EMC	:	Electromagnetic Compatibility
EUT	:	Equipment Under Test
FM	:	Frequency modulation
fs	:	Femto second
GHz	:	Giga Hertz, (10^{9}Hz)
GPIB	:	General Purpose Interface Bus
Hz	:	Hertz
K	:	Kelvin
kHz	:	Kilo Hertz
Log	:	Logarithm
LUF		Lowest Usable Frequency
m	:	Meter
mA	:	Miliampere
MHz	:	Mega Hertz
mm	:	Milimeter
ms	:	Milisecond
mW	:	Miliwatt
nm	:	Nano meter
ps	:	Pico second
RC		Reverberation chamber
RSS		Root Sum Squares
s	:	Second

T	:	Temperature, (K)
THz	:	Tera hertz
TÜBİTAK	:	Türkiye Bilimsel ve Teknolojik Araştırma Kurumu (The Scientific and Technological Research Council of Turkey)
UME	:	Ulusal Metroloji Enstitüsü (National Metrology Institute)
V	:	Volt
W	:	Watt
x		x-direction at cartesian coordinate system
y		y-direction at cartesian coordinate system
z		z-direction at cartesian coordinate system

LIST of FIGURES

LIST of TABLES

1. INTRODUCTION

The first studies on the reverberation chambers in the literature was stated in [1] while the first studies on its application fields were done in [2-8]. The quality factors that constitute an important parameter for the reverberation chambers were studied in details in [9]. Many studies to improve the performance and to extend the usage areas of reverberation chambers in scope of EMI/EMC tests were stated in [10-11], which are valuable studies that can serve as guides. Some of the most recent studies were carried out in [12-16].

The reverberation chambers are able to generate high level uniform electromagnetic fields within, by using the antenna parameters, chamber sizes and low power values applied to their power inputs. Considering the uniformity and low input power advantage, the reverberation chambers provide a significant test environment for EMC/EMI tests and scientific studies. The theoretical electromagnetic field value that is wanted to be generated within the reverberation chambers are determined by using statistical methods. The statistical method is based on using the calibration factors obtained from a few preliminary measurement and calibration processes carried out with the reverberation chambers at the low field levels (for instance, between 20 V/m-100 V/m) to calculate the high level electromagnetic field that is wanted to be achieved. The calibration and measurement procedures stated in the literature are defined by the standards, some of which are stated in [17-20]. Although these standards basically rely on the same calibration methods, test and result analysis stage may provide different results.

We began our study by investigating the differences of the standards that define the calibration methods of the reverberation chambers, in scope of which the correction factors were obtained, which directly affected the targeted electric field value, because of the above mentioned reasons in the first part of the study and we performed the study stated in [21].

The calibration of the reverberation chambers are carried out at low electric field levels by using the electric field probes. The top limit of the field strength that can be measure by the electric field probes is below the high level electromagnetic field strength generated within the reverberation chamber during the test measurements, therefore they are removed from the chamber to protect the electric field probes from damage after the chamber calibration measurements are completed.

Electrical field probes are diode or thermocouple-based dipole antenna structures, of which operation principles are stated in detail in [22-26], and these devices carry out broadband measurement.

The calibration factors obtained from the calibration measurements of the reverberation chambers are used to calculate the field that is going to be generated within the chamber during the DAC (Device Under Test) immunity measurements. This semi-theoretical electrical field strength value cannot be verified experimentally and in real time, because the electrical field probe is removed from the chamber because of the high levels applied during the test, in order to protect the device. In the light of this information, we aimed at being able to verify the theoretical field strength, experimentally and in real time, by using atomic sensors that can sensing the high level electromagnetic field strength in real time, which can exist within the room during the DAC test measurements in addition to the chamber calibration.

At this point, the high volume of the dynamic measurement ranges and the relation with the laser power are very important because of the operation principles that rely on stimulation of the differences between the line of atomic sensor atoms, with the microwave field. Because, if the dynamic operation ranges of the atomic sensors can be optimized with the suitable laser power, it might be possible to use to measure the high level electromagnetic field strength.

Although the dynamic ranges of the atomic sensors are their most important advantages, being able to measure without harmonic by functioning as a frequency selective antenna and having the property of being able to measure with low uncertainty level, are the other significant advantages. Moreover, the atomic sensors that act as frequency selective sensors, and which do not respond to any EM wave other than the targeted frequency and which do not measure or sensing the harmonic and sub-harmonics of the targeted signal, draw the attention by eliminating the harmonic problem which is especially an important problem in high level electromagnetic fields. Eliminating this effect and purifying the system from harmonics becomes much more important as the effects of the harmonics are much more greatly felt in systems such as reverberation chambers, where high level radiation is generated. Thanks to this feature it can be used as a reference calibrator for the reverberation chambers that run at this frequency. Another important advantage of this sensor is, having small size and being made of dielectric materials. Although the sizes of the cylindrical cesium tube used for this thesis study are 2 cm

(length) x 2 cm (diameter), there are smaller cesium tubes available in the market. As it is made of dielectric material, more accurate measurement is possible as no reflection will be caused because of it and the integrity of the measurement area is not affected.

The most important disadvantage of the atomic sensor is the fact that it only runs at 9,192 GHz frequency value within the microwave frequency range. But used frequency spectrum is quite larger during EMC tests and measurements. When this frequency spectrum is extended, the electromagnetic field measurements already carried out in scope of the decade frequencies can still be carried out by using atomic sensor, within a wide frequency spectrum. But the studies on this aspect of the atomic sensor are reserved to the future studies and in this paper we are going to work with an only 9,192 GHz frequency.

The subject draws more interest as the BIPM (International Bureau of Weights and Measures) carries out various projects to redefine SI (International System of Units) units and to base them on universal quantum constants [27]. Moreover, it supports the research projects to obtain electric field and magnetic field strength from the frequency, which is the most accurately measured SI unit. This kind of researches are supported, by the fact that especially during the recent years and BIPM has been planning to implementation to use the atomic sensors were developed in laboratories in electromagnetic test and calibration environments (TEM, Anechoic Chamber, Reverberation Chamber vb.) as stated during the traditional CCEM (Consultative Committee for Electricity and Magnetism) meeting [28].

The first studies in the literature, which constitute the foundations of the atomic sensors, are stated in [29- 35]. Afterwards, scientific studies were carried out to use the atomic sensors as a reference standard for the quantum-based microwave power measurement systems [36-40].

Many valuable experimental studies about how Cs atom reacts when exposed to an external microwave field and which properties come to the forefront when used as a sensor, in other words studies in which Cs atom behavior under external electromagnetic field is characterized, are stated in [41-44]. Many studies where various properties of atomic sensors are investigated, where the behaviors of various gases under electromagnetic field are examined in addition to studies carried out with various methods and approaches to extend the usage areas and to use as a reference

microwave power measurements standard are stated in [45-53].

The state-of-the-art atomic sensors have been improved quickly with each passing day and the frequency spectrums with disadvantages can be increased with various methods [54-56]. It is now being practically used in specific fields of electromagnetic measurements in many studies [57,58].

When we investigate the concepts of most of the studies on DROR, the relation between the Double Radio Optical Resonance (DROR) and the microwave field strength was studied. The changes caused by the changing microwave field strength on the amplitude of DROR were studied in scope of the far field measurements [42-44].

However, the studies on the amplitude of DROR resonance also bring along some disadvantages that may directly affect the measurement results. Some of these advantages are the signal/noise (signal to noise ratio) ratio, optical background noise in the environment, and the saturation effects of the photodiode. In other words the conditions of the measurement environment, the linear operation range of the used photodiode and the measurement system quality significantly affect the measurement results. The measurement carried out with insufficient signal/noise ratio depending on these conditions include such effects noticed in the measurement results. Similarly, when the optical background noise of the measurement environment changes during the measurement, these effects become apparent on the measurement results. Another subject is the linearity of the photodiodes used in detecting the optical absorption. The photodiodes, depending on their semi-conductor material properties, operation linearly within a specific dynamic range of optical power and specific wave lengths. On the other hand, may photodiode saturate at high optical power values and errors occur during the measurements that include this kind of changing optical powers.

On the other hand, working with the bandwidth of DROR instead of amplitude is beneficial in minimizing such errors. Similar to amplitude measurements, the changing microwave field strength also causes changes in the DROR bandwidth. As the resonance bandwidth measurements are going to be carried out on the axis of frequency instead of amplitude; the abovementioned signal/noise ratio, optic environmental noise and photodiode saturation effect etc. factors will be felt less. Because when the bandwidth measurements are performed, the measurement is performed at the points where the signal amplitude is reduced to half. Therefore the

changes in the peak value of amplitude or frequency axis will not have any shift in total or even if it does, it will be felt less as the bandwidth is going to be measured where the amplitude is reduced to half.

It is harder to obtain stability DROR amplitude measurements because of the abovementioned parameters in scope of the sensing high level electromagnetic waves. As the broadening will be felt more at the high microwave field levels, the bandwidth measurements are thought to be significantly beneficial in this scope.

With this purpose, in the second part of the study in scope of the thesis; the relation between the DROR bandwidth and the high level microwave field strength was investigated at the different laser powers and the effects on the dynamic ranges of the atomic sensors were examined difference from the characterization measurements based on DROR amplitude measurements.

For this, firstly the resonances of Cs atom that occur during $6S_{1/2}$ (F = 4) ↔ $6P_{3/2}$ (F = 3, 4, 5) transitions and the Zeeman transitions that occur during degeneration under DC magnetic field were used. A high level electromagnetic field was generated, which changes with steps of 500 V/m, from 500 V/m to 7,5 kV/m in the near field by using a horn antenna at fixed 9,192 GHz frequency within anechoic chamber during the measurements. The relation between the bandwidth of the central Zeeman resonance that occurs on $6S_{1/2}$ (F=3, m_F=0) ↔ $6S_{1/2}$ (F=4, m_F=0) transition of Cs atom and the electromagnetic field strength were examined with power broadening effect at the various laser powers.

In the third and last part of the thesis, a study was carried out for the first time, to use an atomic sensor to measure the high level microwave fields created within reverberation chambers. For this purpose, the double radio optical resonance of atomic sensor generated by the microwave interaction and the Zeeman spectrums occurring under DC magnetic field were tried to be obtained in the microwave field generated within the reverberation chamber. Afterwards, the amplitude and bandwidth measurements of Zeeman resonance and the amplitude measurement of DROR resonance were performed within the reverberation chamber. Usage of the atomic sensor to verify the high level microwave field strengths of the reverberation chambers was evaluated by interpreting the measurement results.

This thesis study consists of three main parts. In the first part, the calibration step of the standards that define how the EMI/EMC tests can be performed with the

reverberation chambers and the differences between the analyses of test results were investigated and the results of the study were discussed.

In the second part, the bandwidth and amplitude measurements of the atomic sensor were carried out at Zeeman sub-levels under microwave field. The atomic sensor properties and dynamic ranges were discussed based on the information obtained from these measurements and the results were shared under the related titles.

In the third and last part of the study, the measurements of the atomic sensor within the reverberation chamber were performed, the measurement results were discussed and shared under the relevant titles.

2. REVERBERATION CHAMBER THEORY, STANDARDS AND EXPERIMENT

2.1. Reverberation Chambers

A reverberation chamber is a highly conductive shielded enclosure used for generating an electromagnetic (EM) environment for conducting RF radiated susceptibility testing and emissions measurements. The operational concept is similar to a very large microwave oven. The introduction of RF energy into a chamber produces complex field structures created by the resonant modes and multipath reflections. The resonating frequencies are determined by the dimensions of the chamber. Rotating mechanical stirrers in a chamber further "mixes" the energy, effectively changing the boundary conditions and generating new complex field structures. The changing multi-moded complex field results in a statistically uniform and isotropic test environment. Mode-stirring and mode-tuning are two of the techniques that can be used in operation of reverberation chambers. During mode-stirring the stirrers continuously rotate at a set rate.

Mode-tuning requires the stirrers to be incrementally stepped through a complete rotation with a set dwell time applied at each step. In either case, one complete stirrer rotation will result in a test environment that is statistically isotropic, uniform, and randomly polarized. The device under test (DUT) is, therefore, exposed to radiation from all aspect angles and polarizations, thus eliminating the need to move or rotate it.

Reverberation chambers offer several advantages compared to anechoic chambers, such as,

- field uniformity and repeatability,
- the ability to generate higher field levels efficiently with less input power,-
- reduced test time due to the isotropic nature of the electric fields,
- and a screened environment with no ambient signals.

The reverberation chamber is associated with a lowest usable frequency (LUF). This is the minimum frequency where a sufficient number of modes are generated to ensure adequate field mixing and uniformity within a chamber. This minimum frequency is influenced by a chamber's size and geometry. The minimum lowest

usable frequency can calculable by using (2.1). If, for a given frequency, N is less than 100 then the chamber should not be used at or below that frequency.

$$N = \frac{8\pi}{3} abd \frac{f^3}{c^3} \tag{2.1}$$

Where:

- a, b, and d are the chamber internal dimensions in meters
- f: is the operation frequency in Hz
- c: is the speed of propagation ($3x10^8$ m/s)

Generally, larger reverberation chambers have a lower minimum usable frequency. In scope of the research TUBİTAK UME reverberation chamber were used, and the dimensions of the reverberation chamber, and lowest usable frequency of it were given in Table 2.1.

Table 2.1. Dimensions of the reverberation chamber and usable lowest frequency of it in TUBİTAK UME EMC Laboratory.

Length (m)	Width (m)	Height (m)	Lowest Usable Frequency (MHz)
4.9	3.6	3	200 MHz

2.2. Reverberation Chamber Standards

Radiated immunity tests in reverberation chambers are commonly performed as per prominent EMC standards such as IEC61000-4-21 [17], DO160F [18], DO160G [19] and MILSTD461F [20]. Although all the relevant EMC standards aim for radiated immunity testing in reverberation chambers, there are differences in analysis and application of calibration and test stages. In addition, despite the fact that there is a good amount of work in literature about reverberation chambers, most of them deal with the deep theoretical part of reverberation chambers rather than the differences of the reverberation chamber standards. There are limited numbers of papers which focus on the standards and their differences. In [59, 60], there is a comparison between reverberation and anechoic chamber measurement results. A few reverberation chamber standards are theoretically compared in [61] in terms of

maximum field strength. In this research, we mainly focused on differences between four prominent reverberation chamber immunity standards instructively; IEC61000-4-21, DO160F, DO160G and MILSTD461F and experimentally emphasized the differences in the test results for the frequency range from 200 MHz to 1 GHz. For this purpose, we began the research with developing a software solution (Visual C++) that covers the "empty chamber", "loaded chamber", "Equipment Under Test (EUT)" calibrations and also the test methods of the all the studied standards. Thereafter, we performed an empty chamber calibration and field uniformity analysis as per all the aforementioned standards. After the calibration and the field uniformity analysis, we carried out a test chain in accordance with each standard and thereafter compared the results. The comparison was simply based on the target forward power levels required and calculated by each standard for the same electrical field target level by means of four types of EUT.

2.3. Experimental Setups and Theory

As per IEC61000-4-21 and MIL-STD461F, the empty chamber calibration and the field uniformity measurement are performed at 8 points with the use of Ex, Ey and Ez readings of the field sensor and readings of the receiving antenna. Unlike IEC61000-4-21 and MIL-STD461F, the calibration is performed at 9 points with the use of the total RSS readings of the field sensor in DO160F and DO160G in addition to E_x, E_y and E_z readings. As a consequence, in the empty chamber analysis, while IEC61000- 4-21 and MIL-STD461F base the final field uniformity result on separate E_x, E_y and E_z readings of the field probe, DO160 F and G standards also use the total (RSS) field in addition to E_x, E_y and E_z readings. On the other hand, in the test procedures of the standards, there are significant differences. IEC61000-4-21 and DO160F rely on empty chamber data and the EUT loading factor to calculate the test forward power and produce the target test field level as given equation (2.2).

$$P_{input\_test} = \left[\frac{E_{Test}}{\overleftrightarrow{E}.\sqrt{CLF}}\right]^2 \tag{2.2}$$

WhereE_{Test} is the desired target field strength (V/m), CLF is the EUT loading factor, $\vec{\vec{E}}$ given in (2.8) in detail is the average of the maximum electrical fields obtained in the measurement points. CLF is easily obtained by the ratio of antenna validation factors (AVF) obtained at 8 or 9 points in the empty chamber and at 1 point in the chamber with the EUT in turn as given in equation (2.3).

$$CLF = \frac{AVF_{Chamber\_with\_EUT}}{AVF_{Empty\_chamber}} \tag{2.3}$$

$$AVF_{Empty\_chamber} = \langle \frac{P_{AveRec\_Empty}}{P_{Input\_Empty}} \rangle_{8\ or\ 9} \tag{2.4}$$

$$AVF_{Chamber\_with\_EUT} = \langle \frac{P_{AveRec\_EUT}}{P_{Input\_EUT}} \rangle_{1} \tag{2.5}$$

Where; AVF_X is the antenna validation factor for the empty chamber and the chamber with the EUT (X: Empty or EUT), $P_{\mathrm{AveRec\_X}}$ is the average receive power obtained from the receiving antenna for the empty chamber and for the chamber with the EUT (X: Empty or EUT), $P_{\mathrm{Input\_X}}$ is the average input power during the validation in the empty chamber and in the chamber with the EUT (X: Empty or EUT). Although both of the standards use the empty chamber data for the test stage, DO160F bases the target test forward power(P_{input_test}) on E_{total} obtained from 9 measurement points as given in equation (2.6, 2.7) and IEC61000-4-21 uses the average of E_x, E_y and E_z readings obtained from 8 measurement points as seen Equation (2.8, 2.9).

$$\langle \vec{\vec{E}}_{Total} \rangle_9 = \frac{\sum \vec{\vec{E}}_{Total}}{9} \tag{2.6}$$

$$\vec{\vec{E}}_{Total} = \frac{E_{Max\_Total}}{\sqrt{P_{average\_input\_chamber}}} \tag{2.7}$$

Where; $\langle \vec{\vec{E}}_{Total} \rangle_9$ is the arithmetic mean across 9 probe measurements, E_{Max_Total} is the maximum measurement (in V/m) from the total E-field from the probe at each location, $\vec{\vec{E}}_{Total}$ is the normalized maximum field (in (V/m) $\sqrt{W}$/),

$P_{average\_input\_chamber}$ is the average input power (in W) to the chamber during the tuner rotation at which E_{Max_Total} is recorded in the empty chamber.

$$\langle \vec{\vec{E}} \rangle_{24} = \frac{\sum \vec{\vec{E}}_{x,y,z}}{24} \tag{2.8}$$

$$\vec{\vec{E}}_{x,y,z} = \frac{E_{Max\_x,y,z}}{\sqrt{P_{average\_input\_chamber}}} \tag{2.9}$$

Where; $\langle \vec{\vec{E}} \rangle_{24}$ is the arithmetic mean across 24 probe measurements$E_{Max_x,y,z}$ is the maximum measurement (in V/m) from each probe axis across all tuner positions, $\vec{\vec{E}}_{x,y,z}$ is the normalized maximum field (in (V/m)/ $\sqrt{W}$), $P_{average\_input\_chamber}$ is the average input power (in W) to the chamber during the tuner rotation at which $E_{Max\_x,y,z}$ is recorded in the empty chamber. On the other hand, for the test stage, DO160G and MIL-STD461 rely only on a simple single-point calibration which is performed just before the test in the EUT presence. In other words, unlike IEC61000-4-21 and DO160F, they do not use the empty chamber data for calculating the test forward power level for the target test field level. Moreover, DO160G and MIL-STD461 themselves also significantly differ from each other. While DO160G uses the received maximum antenna power (P_{rcvmax}) obtained just before the test under the EUT presence to calculate the required forward power for a specific test field value, MILSTD461F alternatively uses the average of E_x, E_y and E_z field probe readings for the same purpose.

$$E_{max} = \sqrt{\frac{377 * 8 * \pi * P_{rcvmax}}{\lambda^2}} \tag{2.10}$$

$$P_{input\_test} = 20 * \frac{E_{test}}{E_{max}} + P_{Fwd} \tag{2.11}$$

DO160G uses equation (2.10) and equation (2.11) based on a one-position just before-test calibration in order to calculate the test forward power level to be used in the test instead of the empty chamber data. Where; E_{max} is the calculated field

strength obtained in the one-position just-before-test calibration in the EUT presence (in V/m), P_{rcvmax} is the maximum recorded power received by the receive antenna over one tuner rotation (in W), λ is the wavelength of the test frequency (in m), $P_{\mathrm{input\_test}}$ is the target test forward power (in W), E_{test} is the desired field strength for the test (in V/m). Ultimately, P_{Fwd} is the forward power obtained in just-before-test calibration at the chamber input in the EUT presence (in W). On the other hand, MIL-STD461F alternatively defines a calibration factor based on $\mathrm{E_x}$, $\mathrm{E_y}$ and $\mathrm{E_z}$ field probe readings in the EUT presence as seen in equation (2.12)

$$CF = \sqrt{\left(\frac{E_{\max\_x} + E_{\max\_y} + E_{\max\_z}}{3}\right)^2 / P_{average\_input\_chamber}} \qquad (2.12)$$

Where; CF is the calibration factor (in V/m for one watt), $E_{\mathrm{max\,x,y,z}}$ is the measured maximum field sensor levels per axis during the tuner rotation$P_{\mathrm{average_input_chamber}}$, is the average forward power measured in the one-position just-before-test calibration during the tuner rotation in the EUT presence. In addition, during the reverberation chamber calibration, it is very important to compare the receiving antenna data and the probe readings to ensure the reliability of the calibration. The discrepancy between the antenna data and the normalized probe data gives an indication of the goodness of the quality of the calibration. Generally, deviations beyond a limit of 3 dB, which can be tolerated up to 4 dB in lower frequencies, point to an issue that should be rectified in the measurement setup. To calculate the delta and perform the verification, the theoretical field calculated from the receiving antenna data given in equation (2.13) is compared with the field results obtained in equation (2.8).

$$\langle \vec{E}_{Receive\ Antenna} \rangle_n = \langle \left(\frac{8\pi}{\lambda} \sqrt{5 \frac{P_{rcv\_max}}{\eta_{rx}}} \right) / \sqrt{P_{input}} \rangle_n \qquad (2.13)$$

Where; P_{rcvmax} is the maximum recorded power received by the receive antenna over one tuner rotation (in W), η_{rx} is the antenna efficiency factor for the receive antenna, which is 0.75 for a log periodic antenna in our case. n is the number of

calibration points in the chamber (n = 8 for IEC61000-4-21 and MIL-STD461F, n = 9 for DO160 F/G). Also, it should be specially stressed that a special maximum loading calibration in the reverberation chamber loaded with absorbers must be performed between the empty chamber calibration phase and the EUT test phase to obtain the maximum loading factor of the chamber. If the loading caused by the EUT exceeds the maximum allowable loading factor, the field uniformity calibration should be repeated and verified in this new higher loading condition because there is not guarantee any more for the field uniformity in this higher loading condition.

In this research, we utilized four EUT types; a large cubic metallic box (70cmx70cm*70cm), a smaller cubic metallic box (20cmx30cm*30cm), a small set of absorbers and a larger set of absorbers which had been also used for the maximum loading test. First, we performed an empty chamber calibration with an input power of 33 dBm at the chamber input port and with a tuner step of 7º, which covers the requirements of all the studied standards for the frequency range from 200 MHz to 1 GHz with a minimum test frequency number of 100 per decade. Thereafter the maximum loading calibration was performed by using the large set of absorbers which was also used as the worst-case EUT later in the test stage. Finally, we performed the tests on all the EUTs in turn and compared the test forward powers calculated and injected into the chamber as per each standard.

2.4. Experimental Results and Discussions

The empty chamber field uniformity and Q factor results are shown in figure 2.1 and figure 2.2. As seen in figure 2.1, the field uniformity indicator which is the standard deviation is below the required limits of the standards for all the cases, except one frequency of the x axis for the IEC limit line.

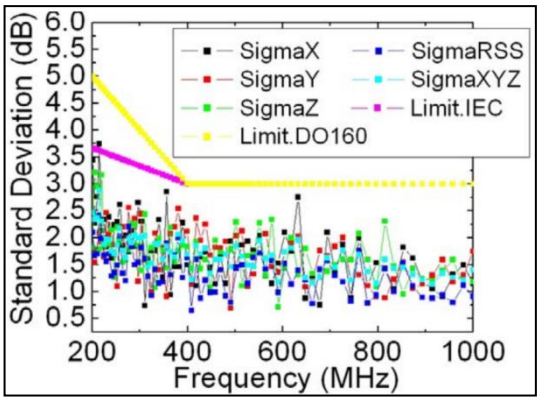

Figure 2.1: Field uniformity measurement results in empty chamber.

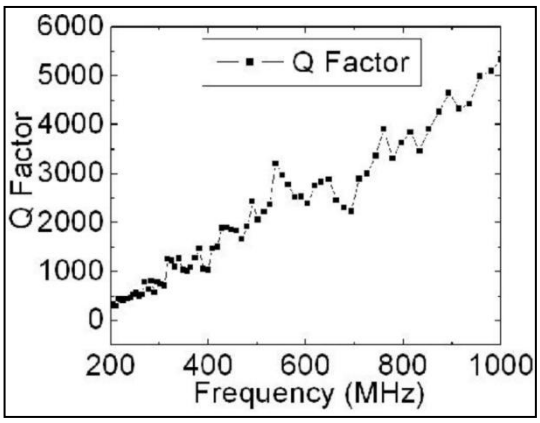

Figure 2.2: Q factor measurement results in empty chamber.

Although it is not stipulated by the standards, we also present the sigma for the RSS field levels in Figure 2.1 just for information. The probe-antenna delta based on the calculation given in equation (2.8), equation (2.13) and the max loading factor measured with the large set of absorbers are given in figure 2.3 and figure 2.4 along with the loading factors of all the EUTs. The delta regarded as the goodness of the quality of the calibration is below 3 dB in most of the frequency range and between 3 and 4 dB only in a few frequencies in the lower frequency range for both of the empty and maximum loaded chamber, which is very satisfactory.

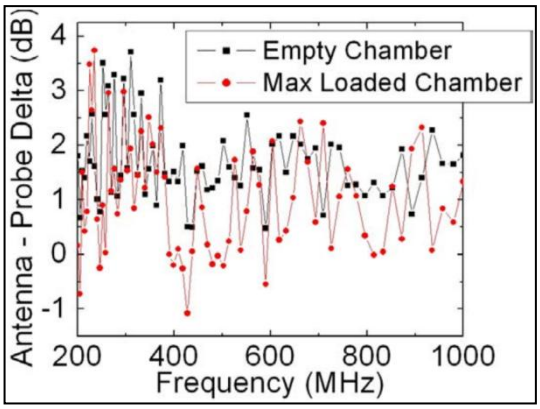

Figure 2.3: Antenna-probe delta values.

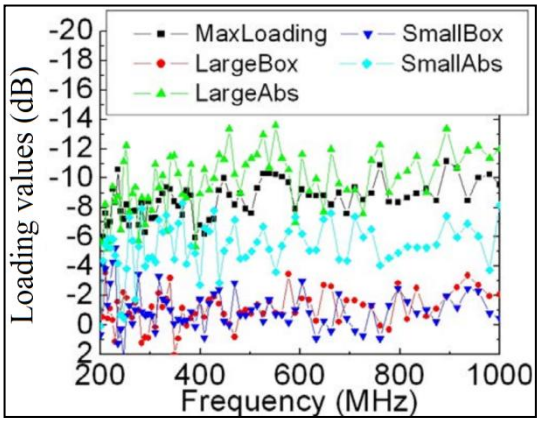

Figure 2.4: EUT loading values.

The maximum allowable loading factor varies from 6 to 10 dB as seen in the figure 2.4. The loading caused by the cubic metal boxes is very close to zero. Even in some frequencies, the loading factors of the metal boxes go below 0 dB, which cannot be possible in fact. This is clearly caused by the fact that the empty chamber AVF_{empty} is measured at 9 points with an average process but the EUT loading (AVF_{EUT}) is measured only in a single-point just-before-test calibration, which gives some uncertainty to the measurement results. On the other hand, the loading factor curve of the large absorber set is almost around the max allowable loading factor, even at most of the frequencies higher than it although the same absorber set is utilized in both of the measurements. This clearly resulted again from the fact that the maximum loading measurement was performed at 9 points with an average process but the EUT loading was measured at a one-point just before-test calibration. Finally, the forward power values calculated as per each studied standard and each

EUT for the same electrical field 20 V/m are presented in figure 2.5-figure 2.8. As clearly seen in the figures, despite the fact that all the standards aim for 20 V/m, the calculated forward power levels in accordance with each standard are significantly different from each other due to the different analysis methods mentioned in the previous section of the paper.

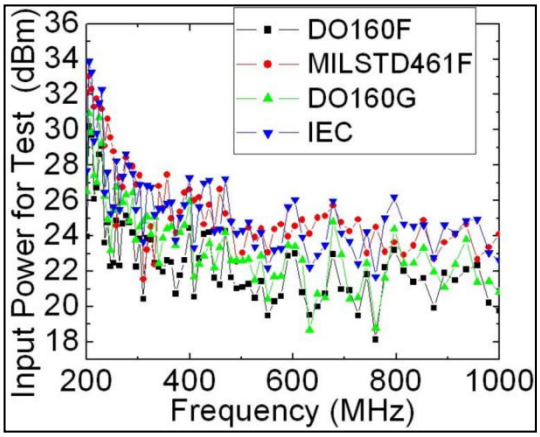

Figure 2.5: Comparison of standards for small metal box.

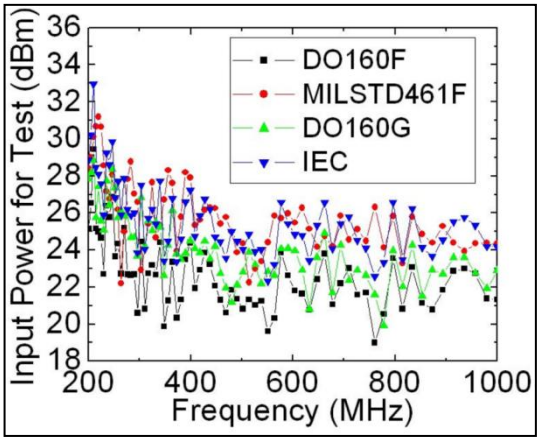

Figure 2.6: Comparison of standards for large metal box.

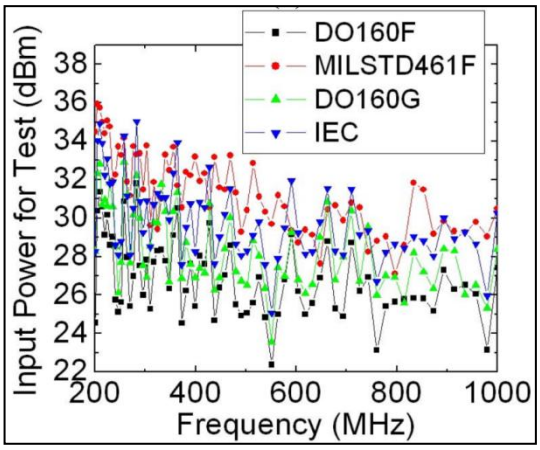

Figure 2.7: Comparison of standards for small absorber set.

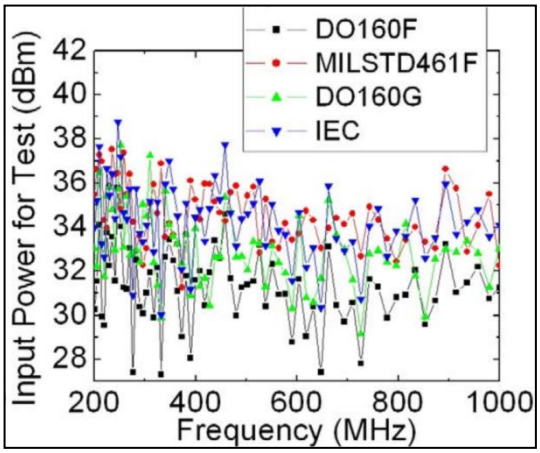

Figure 2.8: Comparison of standards for large absorber set.

When we study the curves in figure 2.5-figure 2.8 in detail, we can generally conclude that MIL-STD461 and IEC61000-4-21 look very similar to each other with an average difference of 0.53 dB but more severe than all the others. DO160F looks like the least severe standard because the input power value required by DO160F is lower by an average deviation of 3.03 dB than the input power values required by IEC61000-4-21 for the same electrical field. Ultimately, DO160G seems less severe than IEC610004-21/MILSTD461 but appears to be slightly more severe than DO160F in our research by an average difference of 1.47 dB. On the other hand, the difference in test results between standards also depends clearly on the EUT loading value and the test frequency.

3. LASER-ATOM-MICROWAVE INTERACTION THEORY AND EXPERIMENT

This part summarizes the theoretical information with the purpose of making the thesis more understandable about the Zeeman effects, Doppler and sub-Doppler resonances, which emerge from the interaction of the laser with the cesium atoms.

3.1. Physical Properties of Cesium Atoms

Cesium atom is one of the alkali atoms in 1A group in the periodic table. Cesium has 55 electrons and only one of them which is in the outermost shell. These metals include one free electron in their last orbit, therefore they can be reduced to hydrogen atom. This free electron is vital in calculating the cesium atom energy levels and transition possibilities. Some of the overall physical properties of neutral cesium atom are given below [65].

Table 3.1: Physical properties of Cesium atoms.

Atomic number	55
Electron number	55
Atom weight	132,905 g/mol
Density at 25ºC	1,93 g/cm^3
Melting point	28,44 ºC
Boiling point	671 ºC
Crystal Structure	Cubic
Vapor pressure at 25 ºC	1,3x10^{-6} torr
Nuclear spin(I)	7/2
Ionization limit	3,89390532 eV
Electronic configuration	$1s^2 2s^2 2p^6 3s^2 3p^6 4s^2 3d^{10} 4p^6 5s^2 4d^{10} 5p^6 6s^1$

3.2. Laser-Atom Interaction

A laser beam is sent at 852 nm wavelength, towards a cylindrical Cs cell made of quartz glass that contains cesium atom. The velocities of the atoms within this Cs cell along any x-direction is determined as in the equation (3.1) based on Maxwell-Boltzmann distribution.

$$N = N_0 \frac{1}{v_0\sqrt{\pi}} \exp\left[\left(\frac{v_x}{v_0}\right)^2\right] \tag{3.1}$$

- N_0 : The maximum quantity of the atoms with average speed, within the Cs .
- v_0 : The maximum average speed of the atoms.

The graphic that shows the speed-dependency of the cesium atoms that interact with the laser beam is stated in figure 3.1 [67].

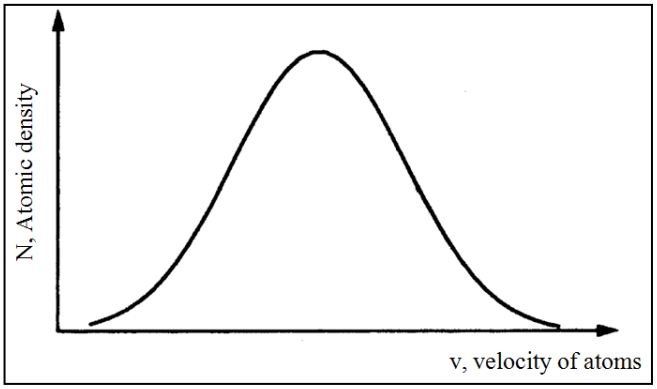

Figure 3.1: The change in the density of atoms according to velocity distributions in scope of Maxwell-Boltzman distribution.

These atoms have E_1 and E_2 ground energy levels as the ground state in the beginning and the first excited state.

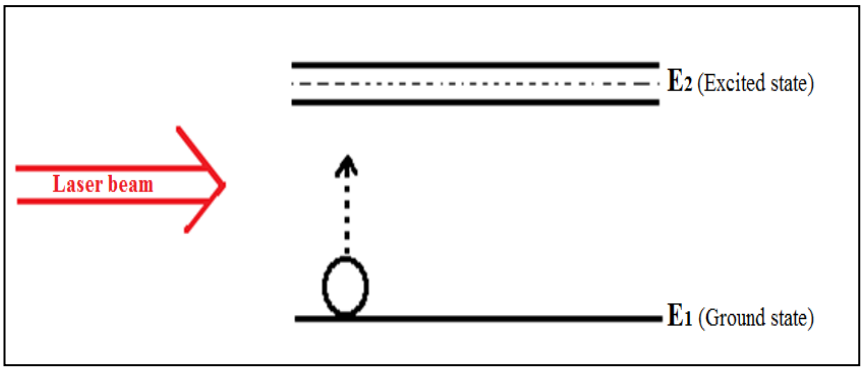

Figure 3.2: Excitation atom with the laser beam.

As seen in Figure 3.2, when the laser beam propagates along x-direction within the cell, the atoms interact with the laser beam. When the laser frequency ωL is scanned in such a way to correspond to E energy transitions, equation 3.2 formula can be written. In this scope the atom at ground energy level will absorb the hωL energy of the photon and were excited from E_1 ground energy level to E2 energy level. The atom that reaches the E_2 energy level will stay there as much as during its natural lifetime (τrad) and later returns to E_1 ground energy level by emitted this photon at any direction.

$$\omega_L = \frac{E_2 - E_1}{\hbar} \tag{3.2}$$

In theory, for an interaction between the laser beam and the atoms to occur, the Cs atoms need to move towards the propagation direction of the laser beam vertically. Cs atoms, which move with v speed under fixed chamber temperature and pressure, will sense the ω_0 frequency of the laser beam with $\vec{k}$ wave vector given in equation 3.5 at different frequencies. Therefore a Doppler shift will happen because of the speeds of the atoms and the laser beam frequency $\overrightarrow{\omega_L}$ will shift from ω_0 frequency given in equation (3.3) where the interaction needs to happen, as much as $\vec{k}.\vec{v}$, based on the rule in equation 3.4.

$$\omega_0 = (E_2 - E_1)/\hbar \tag{3.3}$$

$$\omega_L\text{-}\omega_0 = \vec{k}.\vec{v} \tag{3.4}$$

$$\vec{k} = (2\pi / \lambda)\, \vec{n} \tag{3.5}$$

Where:

- k: Laser light wave vector.
- λ : Laser wavelength.
- $\vec{n}$: Unit vector in the propagation way of the laser beam.
- *h*: Planck constant.

$$\hbar = h / 2\pi \tag{3.6}$$

The average velocity values of the atoms under room temperature is v=3 x 10^4 cm/sn [62]. The atoms can move more than 10 m distance at these temperature values without collision [67], therefore the collisions between the atoms within the cylindrical (2 cm length and diameter) that we use in the experiment, is going to be ignored. The atomic gas density under room temperature is around 3 x 10^{10} atom/cm^3 and the speed distribution is determined with Maxwell – Boltzmann distribution [67]. It can be said that the atoms that are going to interact most with the laser beam will be the atoms with average speed, within the glass cell that contains cesium atoms at fixed laser powers. In this situation, while the laser beam passes through the , the absorption resonance will be maximum at the area where the atoms with average speed are located. When we want to draw this absorption resonance, it will be exactly the reverse marked version of the Maxwell-Boltzman speed distribution. When the laser that passes through the resonance atomic gas, and of which frequency changes as much as ω-$\omega_0 = \vec{k}.\vec{v}$, is sensed by photodiode, a signal absorbed according to the laser frequency change will be sensed on the photodiode. This signal is called the Doppler absorption resonance.

In other words the dependency of the laser power at the exit of the cell on the laser frequency will be as seen in Doppler absorption resonance figure 3.3. The Doppler spectrum corresponds to the speed distribution of cesium atoms at ground energy levels and the line width is around 500 MHz [62].

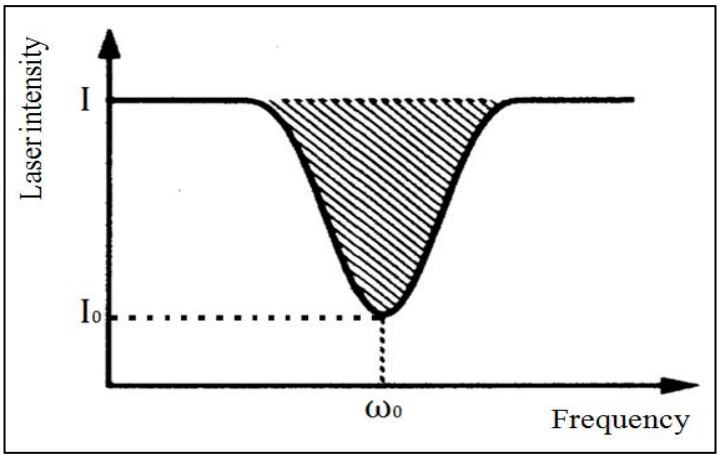

Figure 3.3: Doppler absorption resonance.

A part of the laser beam is absorbed by the atoms as the result of the laser-atomic gas interaction, therefore the laser beam power at the cesium cell exit will always be lower than the power at the entrance, as shown in figure 3.4.

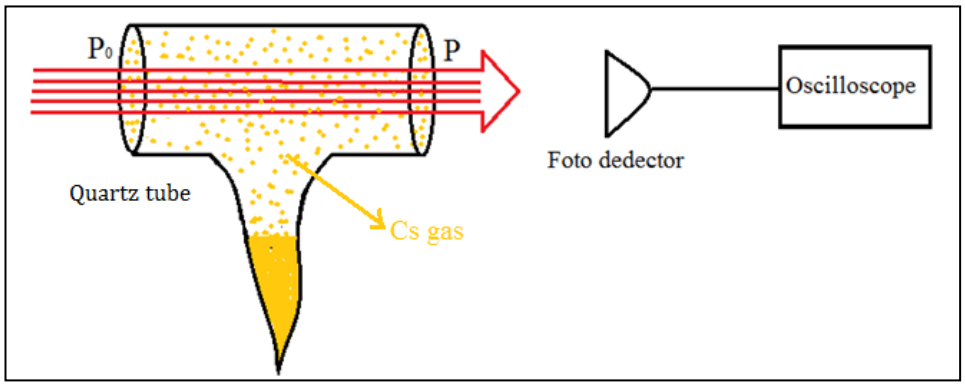

Figure 3.4: Reduction of power along the during the interaction of the laser beam with the resonance atomic gas.

The laser power reduce along the during the interaction of the laser with the resonance atomic gas occurs according to the formula stated in equation (3.7).

$$P = P_0 e^{-\alpha L} \tag{3.7}$$

Here;

- *P:* The laser beam power at the output
- $\boldsymbol{P_0}$: The laser beam power at the input
- *l* : cell length
- $\boldsymbol{\alpha}$: a coefficient depending on the parameters of the laser and the atoms

When the laser frequency is scanned in such a way to include the transitions of $6S_{1/2}$ (F=4) - $6P_{3/2}$ (F =5, 4, 3), the laser beam creates three resonances called hyperfine structures at the lines $6S_{1/2}$ (F =4) - $6P_{3/2}$ (F=5), $6S_{1/2}$ (F=4) - $6P_{3/2}$ (F=4) and $6S_{1/2}$ (F=4) - $6P_{3/2}$ (F=3) which these broadened with Doppler effect. These resonances are called sub-Doppler resonances. The differences between the peaks of the resonances are 251 MHz, 201,2 MHz and 151,2 MHz, therefore this resonance is observed as a single Doppler resonance [63]. These three resonances have different amplitudes. In a situation where the optical pumping is very low, the amplitudes of these resonances depend on the possibility of absorption of the photons by the atom group that corresponds to each line. These transition possibility values are known as 0.45, 0.2, 0.07 respectively for $6S_{1/2}$ (F=4) - $6P_{3/2}$ (F=5), $6S_{1/2}$ (F=4) - $6P_{3/2}$ (F=4) and $6S_{1/2}$ (F=4) - $6P_{3/2}$ (F=3) lines [62]. Therefore the Doppler absorption spectrum that is planned to be experimentally observed will be the total of three spectrums, of which amplitudes are proportional to 0.45, 0.2 and 0.07, and which respectively include 251 MHz, 201,2 MHz and 151,2 MHz between.

The sub-Doppler resonances can be observed with lower uncertainty values by using the saturation absorption spectroscopy method. Therefore the line width of Doppler absorption resonance is required to be examined in detail. Doppler absorption line width is defined by given temperature within the, which is defined with the formula in equation (3.8).

$$\Delta\omega_D = 4\pi\omega_0\sqrt{\frac{2k_BT}{Mc^2}}ln2 \tag{3.8}$$

- k_B : Boltzmann coefficient
- M : atomic mass
- c : speed of light
- T : temperature of the atomic gas

The ω_0 frequency that corresponds to $6S_{1/2}$ - $6P_{3/2}$ energy transitions, which is the D_2 line of cesium atoms, is $\omega_0=5x10^{14}$ Hz. Moreover the Doppler absorption line width for the cesium atomic gas under room temperature (300 K) is $\Delta\omega_D$= 500 MHz.

The difference between the energy transitions of the atoms within the absorption spectrum, of which line width is $\Delta\omega_D$ and central frequency is ω_0 as the result of the interaction between resonance atomic gas and a laser beam with changing frequency and fixed power is, as stated in equation (3.9).

$$E_2 - E_1 = \hbar(\omega_0 \pm \Delta\omega_D) \tag{3.9}$$

Here $\Delta\omega_D$ is the Doppler line width and is actually an uncertainty value and is caused by the velocity distribution of atoms. The saturation absorption spectroscopy method is commonly used to reduce this uncertainty. The interaction of the atomic gas with two laser beams directed face to face at the same moment is used in this method shown in figure 3.5.

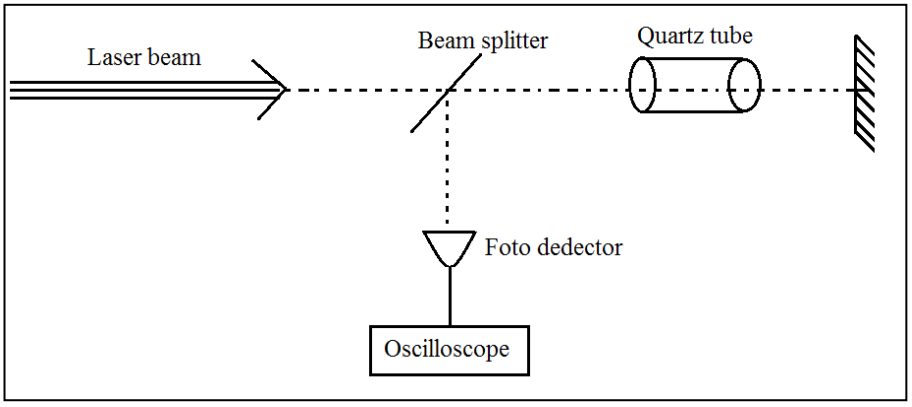

Figure 3.5: Saturation absorption spectroscopy experimental setup block diagram.

In figure 3.5, the laser beam is passed through the quartz tube (Cs cell) and reflected back from the mirror. The reflected laser beam interacts with the atomic gas again and the beam is sensed by a detector via beam splitter. In this setup, the laser transmitted to the glass cell and mirror is called the pumping laser, while the laser that returns from the mirror to the detector is called sensing (probe) laser. The frequencies of the two laser beams sent face to face within the Cs cell are the same but the directions, in other words the wave vectors (+k, -k) are different. Therefore, if the laser frequency is not equal to ω_0 according to the Doppler effect, two laser beams sent face to face will interact with the atomic group that moves with different velocities as in the equation (3.10) and the collapses in figure 3.6 will occur. In this graphic the y axis is $\alpha(\omega)$ and the frequency-dependent absorption coefficient while the x-axis is the frequency axis.

$$v = \frac{\omega_{L-}\omega_0}{k} \tag{3.10}$$

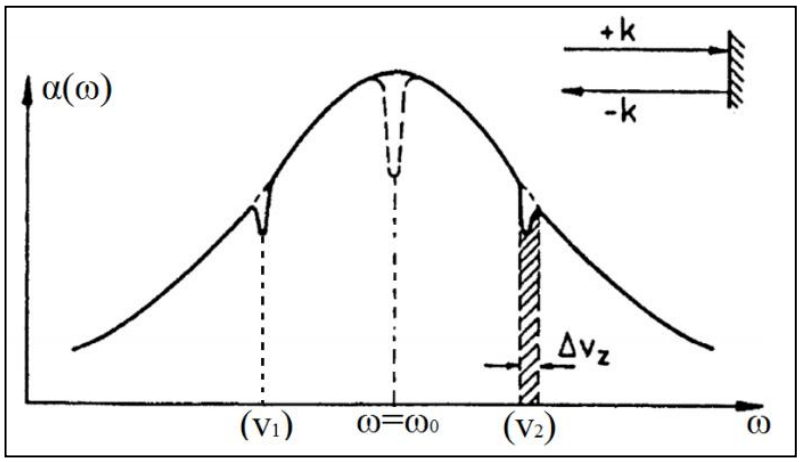

Figure 3.6: Collapse obtained with laser beam on Doppler spectrum.

If the laser frequency is equal to ω_0 ($\omega_L=\omega$) the laser beam in both directions will interact with the same group of atoms (atoms which are in vertical position to the laser beam). The sensing (probe) laser beam transmitted to the detector will interact, at the same time, with the atomic group affected by the pump laser beam transmitted in the opposite direction and the Lamb dip in figure 3.7 will be occurred.

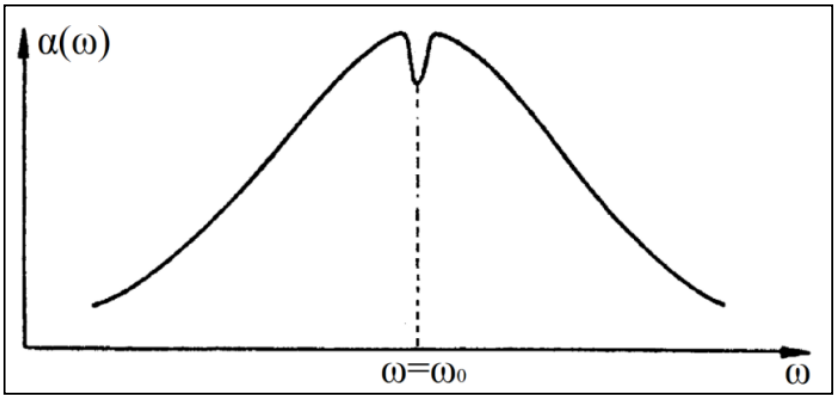

Figure 3.7: The Lamb dip occurring at the resonance frequency ($\omega=\omega_0$) on Doppler absorption spectrum.

As the pump laser beam excite a specific number of atoms to E_2 energy level, the number of atoms sensed by the probe laser beam at E_1 energy level will be reduced. It must be especially emphasized that this interaction has selective character at ω_0 frequency. The bandwidth of this selectiveness will not be defined by $\Delta\omega_D$ but

γ_{rad} . Actually, because of a few physical factors this bandwidth γ is not γ_{rad} but bigger. These are the saturation effect, the angle between the two beams sent face to face, and the collision of atoms. In this case the γ value can be written as in the equation (3.11).

$$\gamma = \gamma_{rad}\sqrt{1+G} + \Delta\omega_D \times \theta + \gamma_{ç} \tag{3.11}$$

The distinct terms that draw attention here, $\gamma_{ç}$ is about the collision of the atoms, θ is the angle between two laser beams and G is the parameter related to the saturation effect. The free flight distance for cesium atoms is known as 300 m for 1 second, the Cs cell length is 2 cm. Therefore the collisions can be ignored and $\gamma_{ç}$ term regarding the collusions in this equation can be ignored. If the two laser beams are adjusted face to face with a very small angle (if $\theta < 10^{-3}$ radian) the broadening caused by the angle will be smaller than 0,5 MHz. If the power of the beams that are sent face to face is low ($G << 1$) in this case the line width of the sub-Doppler resonances (fine structure) obtained according to the equation (3.11) will be γ_{rad}=5 MHz. Consequently, the difference between $E_2 - E_1$ energy levels of the atoms can be correctly obtained with the accuracy in equation (3.12) by using the saturation absorption spectroscopy method.

$$E_2 - E_1 = \hbar(\omega_0 \pm \gamma) \tag{3.12}$$

In scope of the thesis study, the transitions of the cesium atom at D_2 line, 852 nm wave length were used. The transition of the cesium atom, which is called D_2, occurs between the ground energy level $6S_{1/2}$ and upper energy level $6P_{3/2}$. Life time of the valence electron during the transition between these levels is around 30 ns. The visual drawing of the ground and excited levels are shown in figure 3.8.

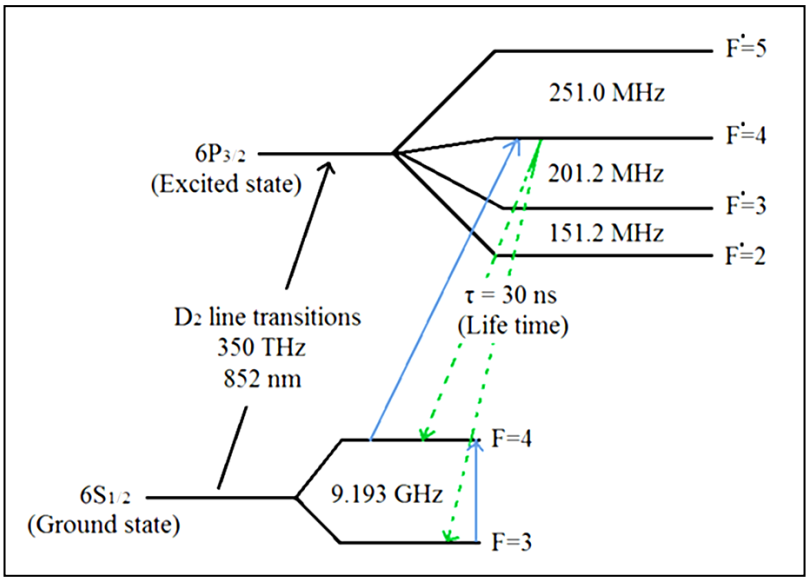

Figure 3.8: Energy transitions on D_2 line of Cesium atom.

The fine and hyperfine structures of the atoms are determined based on quantum mechanics. According to the quantum mechanics principles to obtain the energy transitions on D_2 line for Cesium atom in Figure 3.9, the orbital angular momentum quantum number of the electrons at ground energy level is L=0 (S orbital), while the spin quantum number is S = 1/2. As S>L, the degeneration value is 2L+1=1, in other words there is a only J value, which is J = L + S=1/2. The angular spin momentum quantum number of the atomic nucleus is I = 7/2. As I>J, the number of the possible values of total possible angular quantum number "F"s will be 2J+1=2. The electrons at the ground level will interact with the atom nucleus and the total angular momentum quantum number of the atom will be found as F=I + J and F=|J - I|. Therefore the total angular momentum quantum numbers of the atom will be F = 7/2 + 1/2 = 4 and F = 7/2 – 1/2 = 3 and both sub hyperfine structures will have energy levels $6S_{1/2}$ (F=4) and $6S_{1/2}$ (F=3). The energy difference between these two sub levels correspond to the equation $\Delta E_{4\text{-}3}$= h*9,192 GHz. The microwave interaction of the cesium atoms occurs at this $6S_{1/2}$ (F=3) ↔ $6S_{1/2}$ (F=4) energy transition.

The upper energy level for 6P is S=1/2 and L=1 (P orbital). S<L, therefore the degeneration value will be 2S+1=2, in other words the number of possible values of "J"s is two, therefore two hyperfine structure components will occur as J=|L-S|=1/2 and J=L+S=3/2. In scope of the studies in the thesis we only focused on J=3/2 in other words $6P_{3/2}$ component. The nucleus spin quantum number for an upper energy

level is I=7/2 therefore the number of possible total angular quantum number "F"s is I>J therefore 2J+1=4. These F values will be values with +1 steps between |J-I|=2 and J+I=5. Therefore the upper energy level $6P_{3/2}$ is divided into four sub levels $6P_{3/2}$ (F = 5, 4, 3, 2).

3.3. Laser-Atom-Microwave Interaction

In scope of the thesis study, the laser frequency is locked with the by using a lock-in amplifier in such a way the resonance with biggest amplitude corresponds to $6S_{1/2}$ (F=4) ↔ $6P_{3/2}$ (F=4) energy transition. Therefore the atoms within the glass cell will be raised from $6S_{1/2}$ (F =4) level to $6P_{3/2}$ (F=4) upper level and from that point, spontaneously, some of these atoms return back to $6S_{1/2}$ (F=4) level, while the others return to unused $6S_{1/2}$ (F=3) level. As the result of this optic pumping, the number of atoms at ground level $6S_{1/2}$ (F=4) will be reduced and the laser absorption adjusted from this level to $6P_{3/2}$ (F=4) level will be reduced, too. This absorption that only occurs at the fixed 350 THz (852 nm) laser frequency value becomes balanced within a short time at fixed laser power. In this case the microwave signal is applied on the cesium cell by scanning the frequency at ±10 MHz. When the microwave frequency scanning corresponds to $6S_{1/2}$ (F=3) and $6S_{1/2}$ (F=4) transition and exactly to 9,192631770 Hz frequency, $6S_{1/2}$ (F=3) level atoms absorb the microwave field and excites to upper level $6S_{1/2}$ (F=4). The laser and microwave interaction of Cs atom on D_2 line energy levels is stated in figure 3.9 [62].

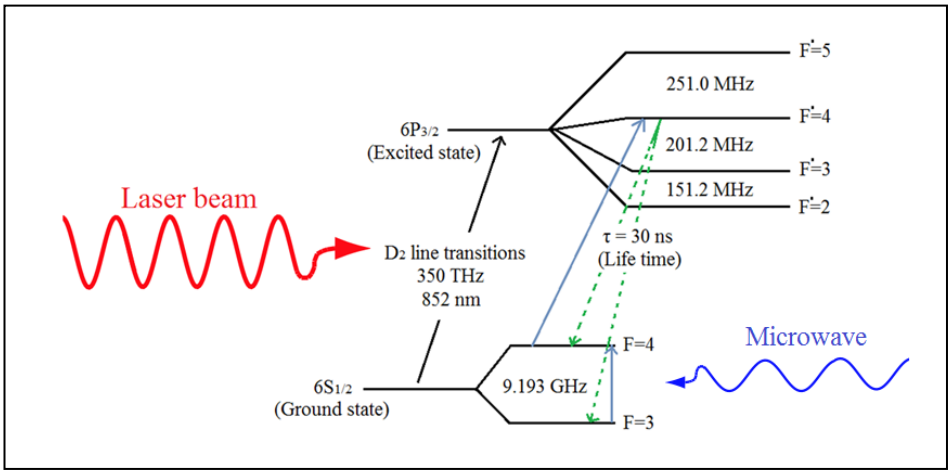

Figure 3.9: The laser and microwave interaction on D_2 line energy levels of Cs atom.

As the result of this transition the number of atoms at $6S_{1/2}$ (F=4) level will be increased, therefore the absorption of the laser fixed to $6S_{1/2}$ (F=4) ↔ $6P_{3/2}$ (F=4) transition will be increased, therefore the resonance amplitude occurring absorbed by cesium atoms of the laser passing through cesium cell will increase. This increase is called the double radio optic resonance (DROR) [63]. The display of DROR resonance on the Doppler absorption resonance is available in figure 3.10.

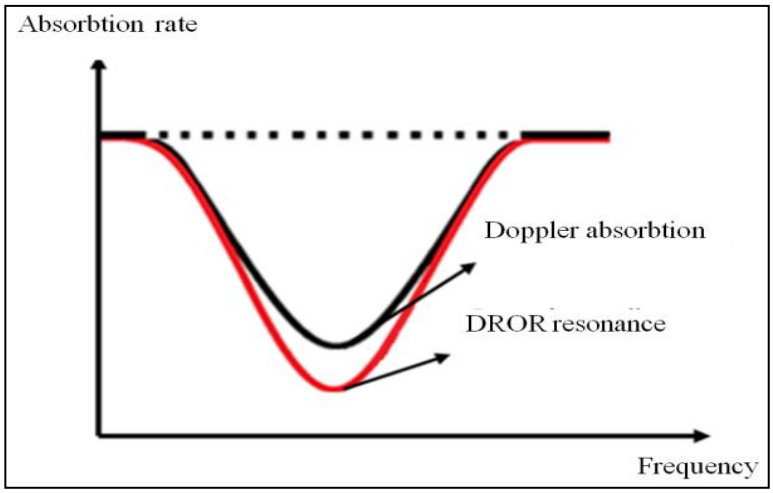

Figure 3.10: The signal of DROR, which occurs when microwave field is applied, on the Doppler absorption resonance.

3.4. Laser-Atom-Microwave Interaction in external DC Magnetic Field

After DROR signal or resonance is obtained, when an additional external DC magnetic field is applied on the cesium atoms, the Zeeman energy splits occur as shown in figure 3.11, which do not normally exist but which emerge as the result of applying external DC magnetic field on the atoms, and which have bandwidths that correspond to kHz or MHz levels. Zeeman sub levels are found with the help of the formula stated in equation (3.13).

$$\Delta E = -g_L \mu_B m_F B \tag{3.13}$$

- g_L: Lande' g-factor
- μ_B: Bohr magneton
- m_F: Magnetic quantum number
- B: DC magnetic field

$6S_{1/2}$ (F=3) ↔ $6S_{1/2}$ (F=4) levels, of which bandwidths that depend on the applied DC magnetic field strength level change, will be splitted into 2F+1 sub energy levels. In this case Zeeman split will occur during F=4 and F'=4 transitions as many as 2F+1=2*4+1=9, in other words at m_F=+4…-4 levels; and during F=3 transition as many as 2F+1=2*3+1=7, in other words at m_t=+3…-3 levels.

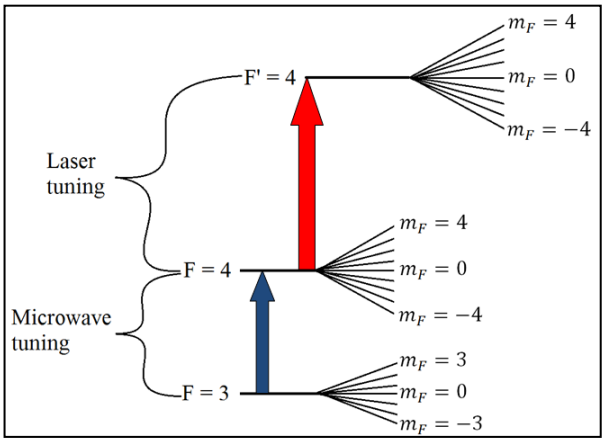

Figure 3.11: Drawing the Zeeman energy levels during on D_2 line of Cs atoms.

The types of the transitions that the occurring Zeeman spectrum is defined according to the rule stated in equation (3.14).

$$\Delta m_F = m'_F - m_F \tag{3.14}$$

Here the Δm_F value can also have Δm_F=0, ±1 values according to the quantum mechanics. It means the valence electron can only perform the transitions, between which 0, ±1 differences occur. If Δm_F=0, the performed transition is named as π-transition; if Δm_F= ±1, the performed transition is named as σ-transition. The

transitions between these Zeeman splits that occur under DC magnetic field, their indexed representative images and transition types are stated in figure 3.12.

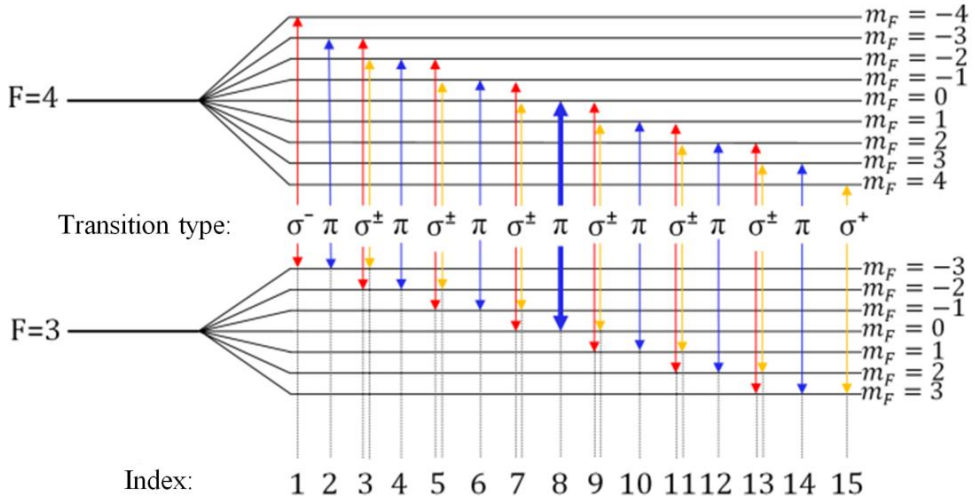

Figure 3.12: Zeeman transitions on the energy levels and displaying the number and types of Zeeman transitions.

Here, 12 of 14 σ-transitions are available as double, as $\sigma^+$and σ^- transitions. The frequency difference between the double $\sigma^{\pm}$ transitions is beyond the frequency resolution that can be sensed by our devices, therefore $14 - 12/2 = 8$ σ-transitions will be observed in total. As seen in figure 13, there are 15 transitions observed in total (8 σ-transitions and 7 π-transitions. All of the Zeeman resonances that occur during $6S_{1/2}$ (F=3, m_F=0) ↔ $6S_{1/2}$ (F=4, m_F=0) transition are indexed and shown in Table 3.2 including the transition types and transition quantities with L_{m_F',m_F} display.

Table 3.2: The index, transition types and quantities for all Zeeman transitions that occur at $6S_{1/2}$ (F=3) and $6S_{1/2}$ (F=4) energy levels.

Index	Transition name	Transition type
1	$L_{-4,-3}$	σ^{-}
2	$L_{-3,-3}$	π
3	$L_{-3,-2}$, $L_{-2,-3}$	$\sigma^{\pm}$
4	$L_{-2,-2}$	π
5	$L_{-2,-1}$, $L_{-1,-2}$	$\sigma^{\pm}$
6	$L_{-1,-1}$	π
7	$L_{0,-1}$, $L_{-1,0}$	$\sigma^{\pm}$
8	$\boldsymbol{L_{0,0}}$	$\boldsymbol{\pi}$
9	$L_{1,0}$, $L_{0,1}$	$\sigma^{\pm}$
10	$L_{1,1}$	π
11	$L_{2,1}$, $L_{1,2}$	$\sigma^{\pm}$
12	$L_{2,2}$	π
13	$L_{3,2}$, $L_{2,3}$	$\sigma^{\pm}$
14	$L_{3,3}$	π
15	$L_{4,3}$	σ^{+}

Here L is the total orbital angular momentum of valence electron. Among these Zeeman sub-energy level splits, $6S_{1/2}$ (F = 3, m_F=0) ↔ $6S_{1/2}$ (F = 4, m_F= 0) is Cs atomic clock transition and the frequency of the clock transition under zero magnetic field is defined as below.

$$\upsilon_0 = 9.192631770 \text{ GHz}$$

In scope of the thesis study, measurements are going to be performed for the high level electromagnetic field applied by focusing on DROR resonance of this $6S_{1/2}$ (F = 3, m_F=0) ↔ $6S_{1/2}$ (F = 4, m_F=0) Zeeman transition. The reason the Zeeman splits are used to sense electromagnetic fields is, the possibility of sensing the small changes in applied electromagnetic field by using the bandwidths of these sub-energy levels. The bandwidth of DROR resonance is much bigger when compared to all Zeeman splits, therefore the small changes within the electromagnetic field are not observable in DROR resonance.

4. EXPERIMENTAL SETUPS, RESULTS AND DISCUSSIONS in AC

In the second part of the thesis study, information will be provided about the setup used for the atomic sensor measurements within the anechoic chamber, the methods of measurement and the measurement results. Afterwards the obtained experimental data is going to be discussed.

4.1. Experimental Setup in AC

The measurement setup basically consists of two main parts including an optical and a microwave part. The optical measurement setup also consists of two parts. The first part of the optic measurement setup is placed on the optical table outside the anechoic chamber, while the second part of the optic measurement setup is positioned within the anechoic chamber. The block diagram of the measurement setup, on which the study was based, is given in figure 4.1.

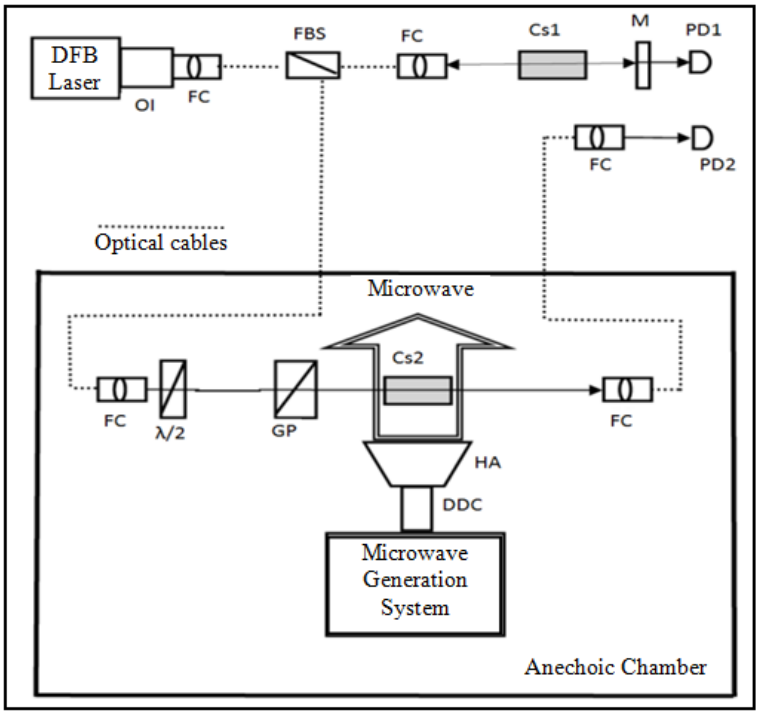

Figure 4.1: The block diagram of the experimental setup, on which the study is based.

The reference Cs1 cell on the optic table outside the anechoic chamber in figure 4.1 is used to display the intra-Doppler resonances. A DFB (Distributed Feedback Laser) laser is used to generate laser beam at 852 nm wavelength on the optic table. DFB laser temperature (25 GHz/K) and current (1GHz/mA) were changed suitably to ensure the laser frequency can scan the $6S_{1/2}$ (F=4) and $6P_{3/2}$ (F′=3, 4 and 5) transition of the cesium atoms. In the setup shown in figure 4.1, generated laser from DFB laser source of Toptica Company's DL100 model was directed towards the FC collimator. The laser light passed through the fiber cable and was split into two at 10/90 ratio by a fiber beam splitter. 10% part of the laser light was sent to reference Cs1 cell while the 90% part was sent to Cs2 cell within the anechoic chamber. A fiber optic-ended FC collimator is used to pass the 10% laser beam through Cs1 cell and a part of it is reflected back by passing through M mirror to observe the sub-Doppler resonances. The returning light and the transmitted light were adjusted sensitively to exactly intersect with each other. The transmitted laser beam is sensed by the first photodiode (PD1). Here the Cs1 reference cell is used for the locking process, of which details will be given later, to generate a fixed laser frequency that does not change in time. Here, the dimensions of the Cs1 cell used for measurements were 7 cm (length) x 2 cm (width). Cs1 cell was the reference cell and was positioned on the optic table outside the chamber, while Cs2 cell was the test sensor with which the measurements would be carried out and was placed within the anechoic chamber.

The laser beam was split into two by FBS in 10/90 ratio, at the first part of the optic experiment setup. Remaining 90% laser light was sent into the anechoic chamber with the help of a 50 m fiber cable with FC-output. This laser beam was passed through the wave plane λ/2 and sent to GP beam polarizer, then through Cs2 cell towards the second photodiode PD2 on the optic table outside the anechoic chamber through 50 m fiber optic cable with FC output. As the measurements were going to be carried out at different laser powers, the optic filters were used for light filtering and optimization processes in front of Cs2 tube and PD2 photodiode entrance.

The fiber cables used for the measurements were single mode cables and they were not polarization maintaining cables. Glan polarizer was used to produce linearly polarized laser light and a more efficient cross section. The diameter of the laser light passing through the cesium cells was adjusted as approximately 5 mm.

During the measurements, DFB laser source temperature (25 GHz/K) and current (1 GHz/mA) were changed suitably to ensure the laser frequency can scan the $6S_{1/2}$ (F=4) and $6P_{3/2}$ (F=3, 4 and 5) transition of the cesium atoms. At fixed laser temperature, DC laser current was modulated at 19 Hz frequency saw signal by using a low frequency signal generator and the scanning range was made observable on the oscilloscope, and in order to this process is called the process of detuning.

For the double radio optic resonance to be observable, the microwave field frequency sent towards the Cs_2 tube (9,192631770 Hz) needs to be applied by being scanned at a specific bandwidth. The scanning process of the microwave frequency is carried out by applying FM (Frequency Modulation) signal. The applied microwave signal scanning corresponds to approx. 20, 85 MHz bandwidth on DROR signal.

In the setup shown in figure 4.1; the cesium tube surrounded by DC Helmholtz coil, the horn antenna and the fiber heads that allow laser entries/exits were positioned within the anechoic chamber while the laser and microwave sources and all other related electronic devices were positioned outside the chamber.

The microwave generating part of the setup includes a microwave signal generator, a microwave power amplifier with 500 W output power, the dual directional coupler (DDC) as shown in figure 4.1 and the standard-gain horn antenna (HA). The power values are measured via the directional coupler called DDC in order to measure the net power at the horn antenna entrance and to create a controlled electric field on the cesium test tube. The electric field value generated at the point where Cs_2 tube is located, the known net power and the known antenna gain, are roughly and theoretically calculated by using the formula in equation (4.1). To generate the maximum electromagnetic field, the distance between the cesium test tube (Cs_2) and the horn antenna end was adjusted as 12 cm approximately. The near field configuration is selected like this to simulate the field environment within the reverberation chamber.

$$E = \frac{1}{d}\sqrt{\frac{n_0 P_{net} G}{4\pi}} \tag{4.1}$$

Here the η_0 is the free space characteristic impedance 377 Ω , Pnet (W) is the net power value at the antenna entrance and d (m) is the distance. The cesium test tube

was placed of the horn antenna frontal end center, at 120 cm height from the ground. Here, the antenna size is D ≈ 12 cm and λ ≈ 3,3 cm (f = 9,192 GHz).

The detailed setup used in the study, which constitutes the microwave generation system part within the anechoic chamber, is shown in figure 4.2.

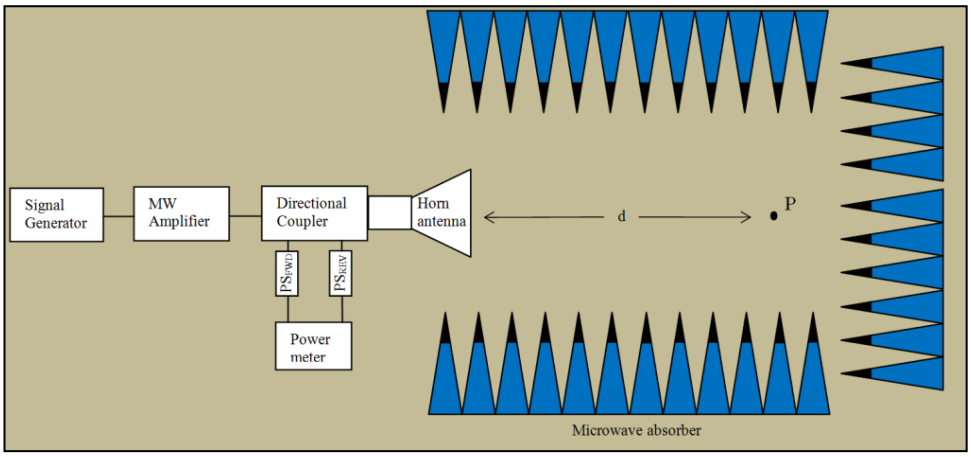

Figure 4.2: Microwave generation part of the measurement setup.

As the microwave was applied, DROR signal was observed on the Doppler signal obtained from the test tube (Cs2). During this observation the laser frequency was adjusted in such a way to scan $6S_{1/2}$ (F=4) and $6P_{3/2}$ (F´=4) transition and the microwave to scan 9,192 GHz central frequency.

DC power source, Helmholtz bobbins and a resistance of 0,5 Ω were used at the part the DC magnetic field was generated and where the measurement setup Zeeman transitions were obtained. The voltages measure via 0,5 Ω resistance by using multimeter were recorded at the magnetic field value required to appear the Zeeman splits. The diameter of the Helmholtz coil used to generate DC magnetic field and the distance between the coils is 18 cm.

The microwave generation part of the measurement setup and all of other measurement devices (oscilloscope and signal generators etc.) are all computer controlled systems. Also a temperature control system was used in the setup to keep the Cs2 tube temperature fixed and to get instantaneous temperature information.

During the measurements within the anechoic chamber, the laser light was polarized linear and the cesium tube was positioned in the near field of the antenna, at approximate 12 cm distance from the vertically polarized horn antenna. The

measurements of the high level electromagnetic waves were carried out in continuous wave mode by using this method.

The sample view from the measurement setup in the anechoic chamber is shown in figure 4.3.

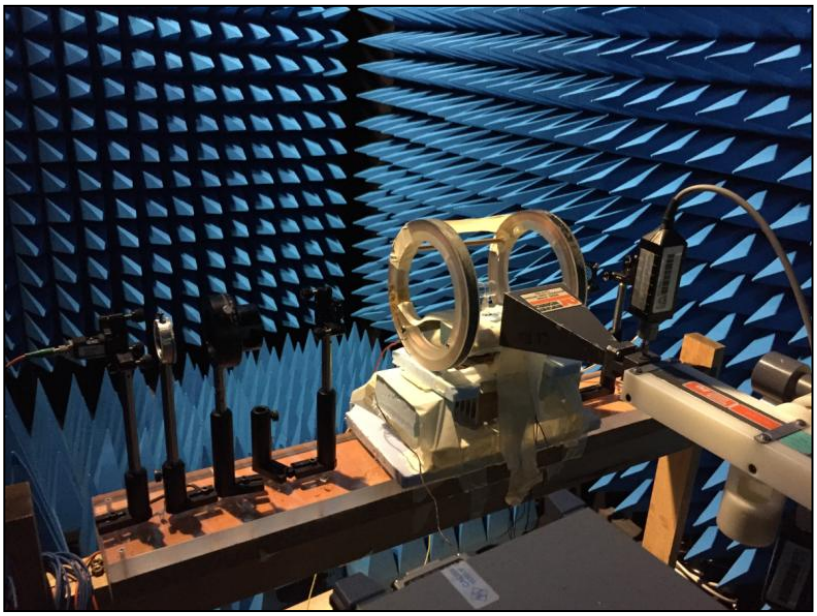

Figure 4.3: The view of the measurement setup within the anechoic chamber.

During the resonance interaction the laser, drives the Cs atoms from $6S_{1/2}$ (F=4) energy level to $6P_{3/2}$ (F=4) excited level. The excited atoms perform transition again to $6S_{1/2}$ (F=4) and $6S_{1/2}$ (F=3) ground state with spontaneous emission. Consequently; although this interaction reduces the number of atoms at $6S_{1/2}$ (F=4) level, the number of atoms at $6S_{1/2}$ (F=3) increases. When microwave is applied, the atoms are driven from $6S_{1/2}$ (F=3) level to $6S_{1/2}$ (F=4) level again. When the applied microwave field amplitude is increased, the atoms at the $6S_{1/2}$ (F=3) level will transition again to $6S_{1/2}$ (F=4) level, therefore it is expected that the atom population at $6S_{1/2}$ (F=4) level will increase with the DROR resonance as the result of the optical pumping, therefore the photon absorption will also increase.

After all these processes, as shown in figure 4.4 and figure 4.5, the Doppler spectrum and intra-Doppler resonances were observed via the Cs1 (cell 1) on the oscilloscope screen, while only the Doppler spectrum is observed via the Cs2 (cell 2). The Cs1 cell was used for the purpose of controlling the locking process during the measurement.

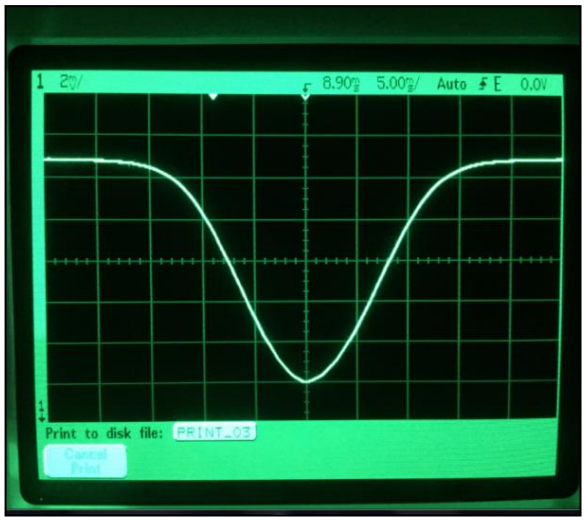

Figure 4.4: Doppler absorption on the oscilloscope display for reference Cs1 tube.

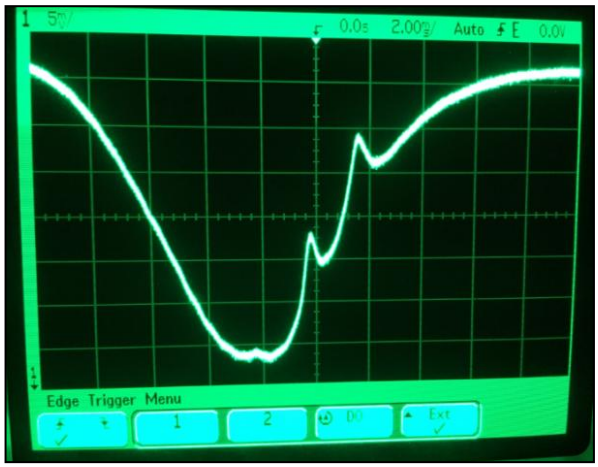

Figure 4.5: Sub-Doppler resonances in reference Cs1 tube displayed on oscilloscope.

The Doppler absorption obtained from the reference cell (Cs1) in figure 4.4 is less than the one obtained within the test tube (Cs2). Because only 10% of the total transmitted laser was sent to the reference tube while 90% was sent to the test tube. The oscilloscope image of the Doppler spectrum observed on Cs2 tube is shown in figure 4.6.

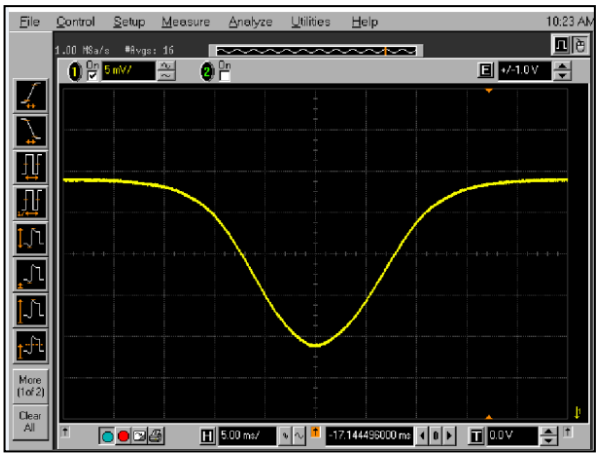

Figure 4.6: Doppler absorption signal of Cs2 test tube.

DFB laser that scans the $6S_{1/2}$ (F=4) and $6P_{3/2}$ (F′=3, 4 and 5) transitions will shift in time because of the current and temperature changes, therefore the laser frequency was locked onto $6S_{1/2}$ (F=4) and $6P_{3/2}$ (F′=4) transition by using a lock-in amplifier. The laser signal passing to through the Cs1 cell was sent to the photodiode, and the signal at the output of the relevant photodiode with a reference sinus signal to the lock-in device (Stanford Research Systems, SR830 model DS Lock-In Amplifier) used for the locking process. The lock-in device received the firsth derivative of the laser signal coming from the reference tube. This signal is the laser frequency changing by the time and is called the error signal [64]. This signal, of which derivative was obtained, was connected to the oscilloscope (Agilent Technologies, model 54624A) to change the signal and optimize the lock-in device multiplier value. Afterwards, the phase of this error signal was changed, in other words reversed with the lock-in device and was sent to the DL100 model source mode input entrance of the DFB laser with the help of BNC cable. Here, 20 dB attenuator was used at DFB laser mod input or locking device output. In this way DC signal that corresponds to laser frequency change was reversed and sent back to the laser, therefore the laser frequency became fixed and the shifts were eliminated with the help of the feedback signal. Consequently the laser frequency locked on $6S_{1/2}$ (F=4) and $6P_{3/2}$ (F=4) transition by using this method. The Doppler signal locked on $6S_{1/2}$(F=4) – $6P_{3/2}$(F=4) transition that does not change with time on Cs1 reference tube and the error signal (below) are shown in figure 4.7 while the Doppler signal locked on $6S_{1/2}$(F=4) – $6P_{3/2}$(F=4) transition that does not change in time on Cs2 reference tube is shown in figure 4.8.

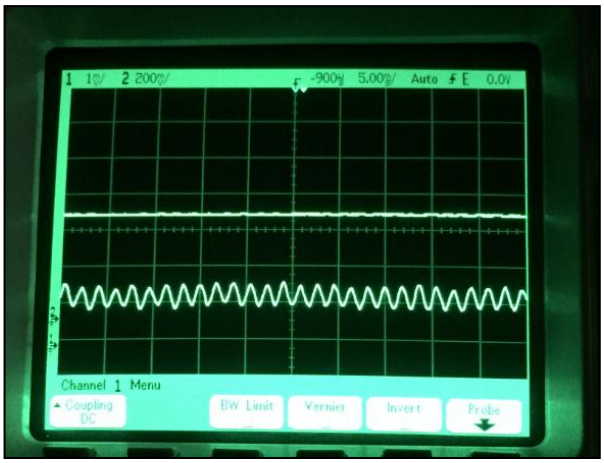

Figure 4.7: The Doppler signal (top) locked on the $6S_{1/2}(F=4) – 6P_{3/2}(F=4)$ transition that does not change with time, on Cs1 reference tube and the reversed error signal (bottom).

Figure 4.8: The Doppler signal locked on $6S_{1/2}(F=4) – 6P_{3/2}(F=4)$ transition that does not change with time, on Cs2 reference tube.

After all of these processes carried out in the setup that constitutes the optic part in scope of the study, the optic setup becomes ready for microwave field interaction at 9,192 GHz.

A few field sources were used in the study, therefore to make the vector direction of all of these fields easier to understand, it is shown on Cs2 test tube as in figure 4.9.

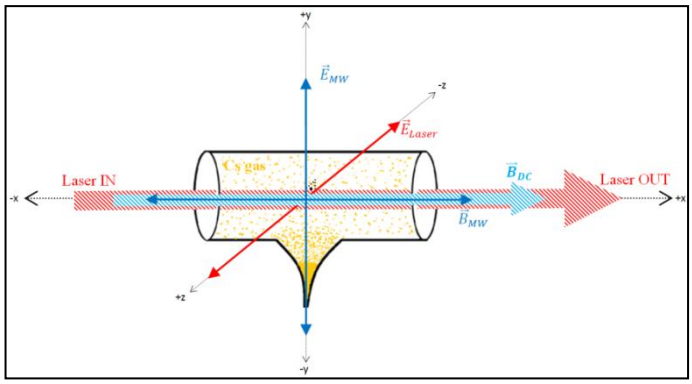

Figure 4.9: Electromagnetic field and laser polarizations on Cs2 test tube.

4.2. Results and Discussion in AC

During the measurements the reference Cs2 cell was placed within a peltier-controlled system, its temperature was kept fixed and the fluctuations in the measurements can be explained with the slight temperature fluctuations caused by the microwave in cesium cell, despite of peltier. The cesium atoms within the cell were both in gas and solid (metal) states. When the cell was subjected to the microwave, the metallic part was heated and vaporization increased, and the increase meant more atoms to absorb more photons, therefore slight fluctuations occurred.

While the environmental temperature during the measurements were (22±2) ºC the cesium tube temperature was tried to be kept at (27±2) ºC by using the peltier-controlled temperature system. Therefore an uncontrolled temperaure increase that could arise from the microwave was prevented.

In order to observe the DROR resonance, the laser frequency was locked on $6S_{1/2}$ (F=4) – $6P_{3/2}$ (F´=4) transition and CW (continuous wave) microwave frequency was scanned with FM modulation in central 9,192 GHz frequency ± 10 MHz range that corresponds to $6S_{1/2}$ (F=3) - $6S_{1/2}$ (F=4) energy transition. The atoms at $6S_{1/2}$ (F=4) ground energy state absorbed the laser and rose to $6P_{3/2}$ (F´=4) excited energy level and emitted spontaneous emission for a short time and dropped to back $6S_{1/2}$ (F=3) or $6S_{1/2}$ (F=4) ground energy level. Therefore this interaction reduced the number of atoms at $6S_{1/2}$ (F=4) level but increased the number of atoms at $6S_{1/2}$ (F=3) level. When the microwave was applied just at this moment, the atoms at $6S_{1/2}$ (F=3) level were started to be excited to $6S_{1/2}$ (F=4) level and with the microwave effect, the number of atoms at $6S_{1/2}$ (F=4) level was increased and consequently the number of atoms that interact with the laser was increased. Therefore the laser lost

more energy and the DROR signal experimentally measured at figure 4.10 was observed. By definition, DROR is the name of the resonance obtained as the result of the interaction of laser, microwave and atoms. The laser excites the atoms during the DROR process within $6S_{1/2}$ (F=4) – $6P_{3/2}$ (F´=4) energy transition while the microwave excites the atoms within $6S_{1/2}$ (F=3) - $6S_{1/2}$ (F=4) energy transition. In scope of the DROR signal in figure 4.10, the laser polarization was kept horizontal and microwave polarization was kept linear (vertical).

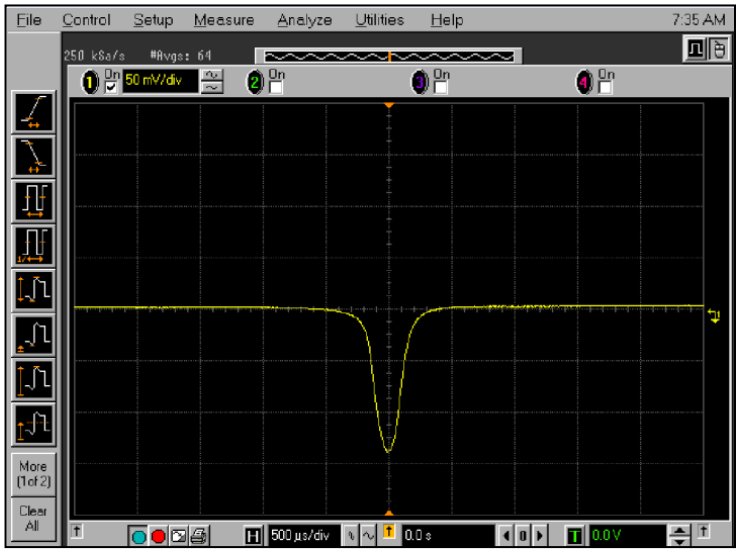

Figure 4.10: DROR resonance for 5 kV/m appearing @3,2 mW laser power on oscilloscope display.

During the resonance interaction, the laser beam electric field drove Cs atoms from $6S_{1/2}$ (F=4) energy level to $6P_{3/2}$ (F=4) excited level, then the excited atoms dropped again to $6S_{1/2}$ (F=4) and $6S_{1/2}$ (F=3) ground state with spontaneous emission. Because of this, although the number of atoms were reduced at $6S_{1/2}$ (F=4) level, the number of atoms at $6S_{1/2}$ (F=3) level increased. When microwave was applied, the atoms were driven from $6S_{1/2}$ (F=3) level to $6S_{1/2}$ (F=4) level again. When the applied microwave field amplitude was increased, the atoms at the $6S_{1/2}$ (F=3) level performed transition again to $6S_{1/2}$ (F=4) level, therefore the atom population at $6S_{1/2}$ (F=4) level increased with the DROR resonance as the result of the optic pumping, and consequently the photon absorption increased. It would be benefit at the drawing the attention to here, high laser powers may cause reverse pumping effects, and may decreased DROR signal amplitude after a while at mentioned transitions.

In scope of the thesis, before starting the Zeeman measurements; DROR signal shapes were obtained at fixed laser power and the fixed cell temperature (T=27ºC) under increasing microwave field, in order to see the effects microwave field on the DROR signal shape.

All of these measurements were carried out at the horizontal polarization of the laser light and the horizontal polarization of microwave magnetic field component.

The image showing the changes that occur with the increasing microwave field of DROR resonance that perform on $6S_{1/2}$ (F = 3) ↔ $6S_{1/2}$ (F = 4) transition is given in figure 4.11.

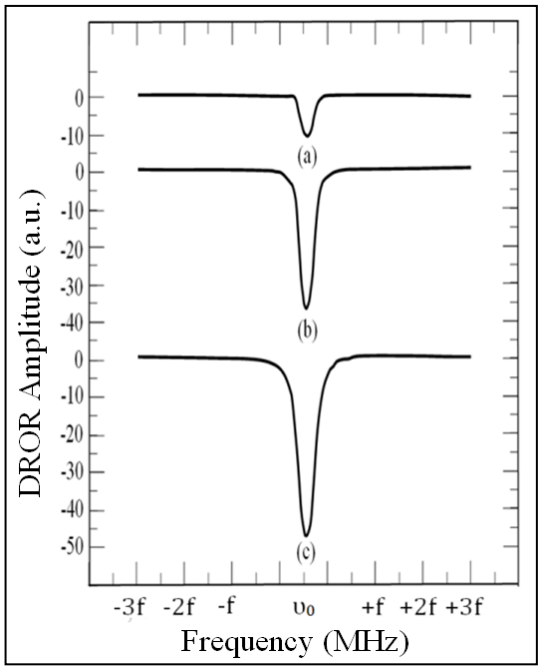

Figure 4.11: DROR signals of $6S_{1/2}$ (F=3) ↔ $6S_{1/2}$ (F=4) transition for various microwave field levels at 3,2 mW fixed laser power, (in horizontal axis υ_0≈9,192 GHz and f≈10 MHz) (a) 1 kV/m electric field strength, (b) 5 kV/m electric field strength, (c) 7,5 kV/m electric field strength.

As seen in the figure 4.11, the increasing microwave field increased the atom population between the $6S_{1/2}$ (F=4) ↔ $6P_{3/2}$ (F=4) levels where the laser was used, therefore we observed a amplitude increasing of the DROR resonance signal together with the increasing microwave field strength.

The microwave field levels to use within the anechoic chamber in scope of the thesis was determined as 500 V/m as the bottom limit and 7,5 kV/m as the top limit. 500 W microwave power amplifier started to generate harmonics and have been

saturate after -10 dBm. That is why the top limit was limited at 7,5 kV/m value. But more powerful microwave power amplifiers can be used to easily increase this level.

DC magnetic field was also applied with the help of Helmholtz coil to measure the amplitude and bandwidth changes that occurred in scope of the Zeeman splits despite of the increasing microwave fields, which was the main subject to study in scope of the thesis. The DC magnetic field direction was kept in parallel towards the microwave magnetic field and laser propagation direction.

The Helmholtz coil used to generate DC magnetic field had a diameter of 18 cm. and distance and was fed by a DC current source via 0,5 ohm resistance. A calibrated magnetometer was used to measure the static magnetic field value at the center of Helmholtz coil that generated static magnetic field before the measurements. After this measurement, the cesium tube was placed on its normal position and Zeeman components were produced with the static magnetic field and later the dependency of these components on the microwave power was investigated.

The Zeeman spectrum generated from DROR signal at fixed laser power under fixed DC magnetic field to visually display the change with the increasing microwave field of the total Zeeman components that occurred during $6S_{1/2}$ (F=3) ↔ $6S_{1/2}$ (F=4) transition with the applied DC magnetic field is shown in figure 4.12. During this measurement the microwave signal generator (Agilent Technologies, E8257C model) was scanned in CW mode in such a way the center corresponds to 9,192 GHz, around ± 10 MHz. The displayed spectrums were recorded at 3,2 mW fixed laser power and under fixed static magnetic field, respectively in 1,5 kV/m, 3 kV/m and 7 kV/m microwave fields.

7 dominant resonance figures that correspond to $6S_{1/2}$ (F=3, m_F=0) ↔ $6S_{1/2}$ (F=4, m_F=0) and ∇m_f=0 transitions are shown in figure 3.26. There were σ-type resonances that corresponded to $\nabla m_f \neq 0$ transitions although not significant among the 7 π-type resonances that corresponded to ∇m_f=0 transitions. The sigma resonances may occur because of the slight environmental reflections or because of not having exact linear polarization for the EM radiation at the horn antenna output.

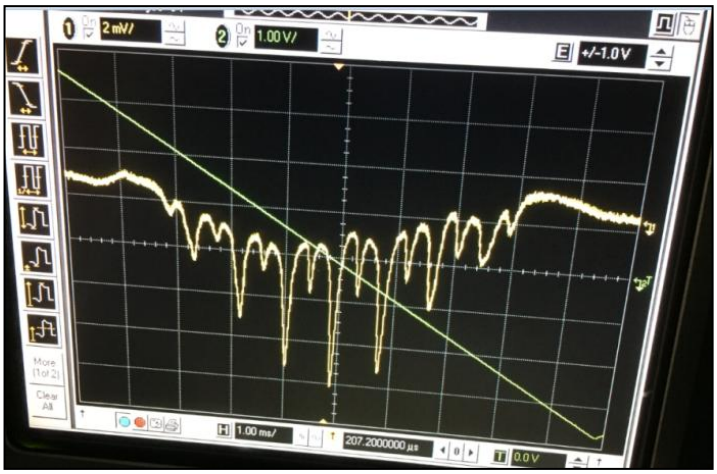

Figure 4.12: Zeeman sublevels of the DROR resonance on oscilloscope display.

In this measurement the horn antenna was placed to near field conditions and the polarization was selected as vertical. Normally in this configuration we were supposed to observe 7 Zeeman components corresponding to only 7 π-transitions, but because of the reflections from the metallic wires of RF Helmholtz coils and other reflections, the total microwave polarization transformed from linear polarization to elliptic polarization. The elliptically polarized microwave causes both the π and σ transitions between $6S_{1/2}$ (F=3) and $6S_{1/2}$ (F=4) energy levels.

The change that occurred in the total Zeeman components that appear during $6S_{1/2}$ (F=3) ↔ $6S_{1/2}$ (F=4) transition with the increasing microwave field, is shown in figure 4.13. The Zeeman component levels increased with the increasing microwave field as shown in Figure 4.13.

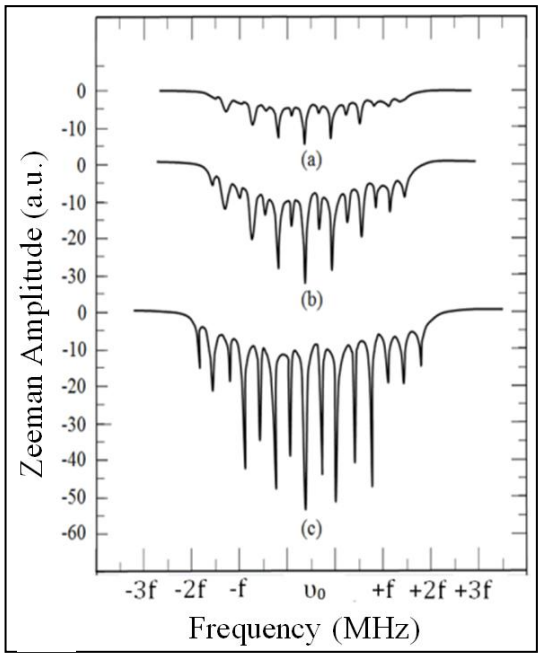

Figure 4.13: 15 Zeeman resonances observed during $6S_{1/2}$ (F=3)↔$6S_{1/2}$ (F=4) transition at 3,2 mW fixed laser power for different microwave field strengths (in horizontal axis $\upsilon_0 \approx 9{,}192$ GHz and f≈10 MHz) (a) 1,5 kV/m electric field strength, (b) 3 kV/m electric field strength, (c) 7 kV/m electric field strength.

12 of 14 σ-transitions in the spectrum shown in Figure 4.13 existed as pairs and their frequencies were very close to each other. As the frequency between the components of each pair is very little, 8-σ transitions were observed on the oscilloscope screen instead of 14. Together with the 7 π transitions, 15 transitions in total were observed on the oscilloscope screen.

The Zeeman component that was wanted to be measured in scope of the thesis study was $6S_{1/2}$ (F =3, m_F=0) ↔ $6S_{1/2}$ (F =4, m_F=0) π-transition. When the static magnetic field value was sufficiently increased, the frequency difference between each Zeeman component in the Zeeman spectrum was increased but the amplitudes stayed the same [42-44]. The energy difference between the Zeeman levels is in the frequency scale and the bandwidth is approximately in scope of kHz or MHz range. Increasing DC magnetic field increase the bandwidth of the Zeeman resonances, and the other Zeeman components stayed out of the scope of the microwave scanning range excluding the central Zeeman component corresponding to $6S_{1/2}$ (F=3, m_F=0) ↔ $6S_{1/2}$ (F=4, m_F=0) π-transition which place no change as it was at the center stayed (figure 4.14).

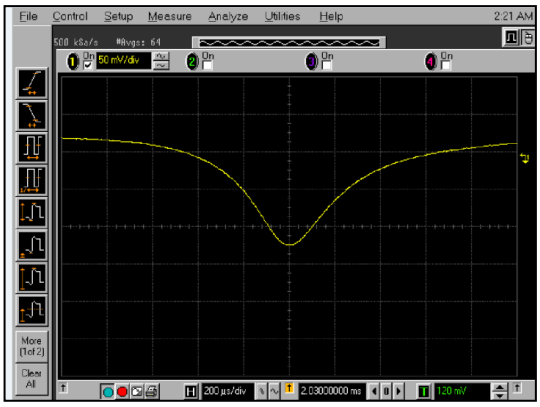

Figure 4.14: The oscilloscope display of central Zeeman component (Index=8) for $6S_{1/2}$ (F = 3, m_F=0) ↔ $6S_{1/2}$ (F = 4, m_F= 0) π-transition at 5 kV/m electric field strength @3,2 mW laser power.

The image of the change and the increasing microwave field of central Zeeman component that occurred at $6S_{1/2}$ (F = 3, m_F=0) ↔ $6S_{1/2}$ (F = 4, m_F= 0) π-transition was shown in figure 4.15 at fixed laser power and approx. 1100 μT fixed DC magnetic field. As shown in Figure 4.15, the microwave field amplitude increased and at $6S_{1/2}$ (F = 3, m_F=0) ↔ $6S_{1/2}$ (F = 4, m_F= 0) π-transition the Zeeman component amplitude and line width increased.

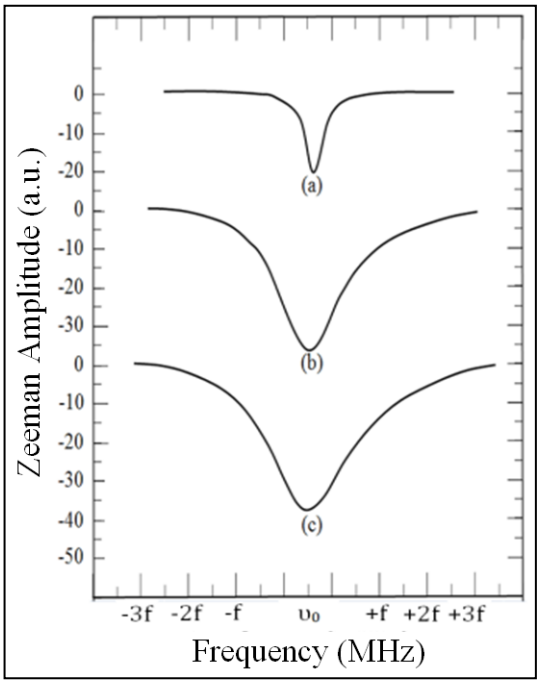

Figure 4.15: Amplitude change of the $6S_{1/2}$ (F=3, m_F=0) ↔ $6S_{1/2}$ (F=4, m_F= 0) π-transition @ 3,2 mW fixed laser power (in horizontal axis υ_0≈9,192 GHz and f≈2 MHz) (a) 1 kV/m field strength, (b) 5 kV/m electric field strength, (c) 7 kV/m electric field strength.

In scope of the thesis study, the dependency of central Zeeman component with $6S_{1/2}$ (F=3, m_F=0) ↔ $6S_{1/2}$ (F=4, m_F=0) π-transition on the microwave field was investigated. The amplitude and bandwidth measurement results for the central Zeeman component that corresponded to the microwave field were shown in figure 4.16 and 4.17. As seen in the measurement results, the increase in the microwave field increased the bandwidth and amplitude of the Zeeman component of the DROR signal.

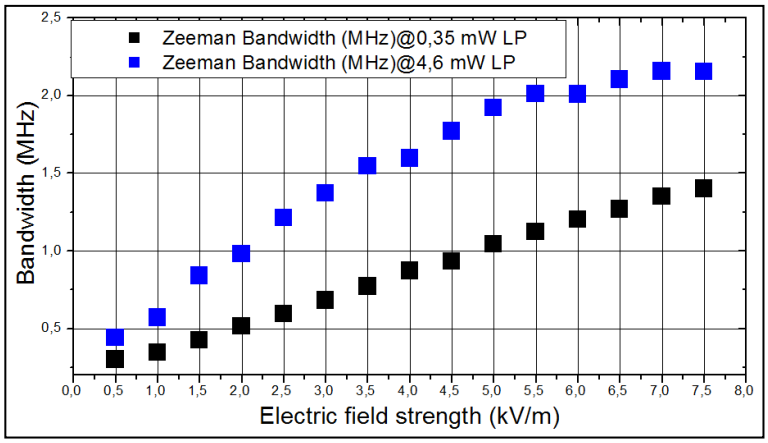

Figure 4.16: The dependency of $6S_{1/2}$ (F=3, m_F=0) ↔ $6S_{1/2}$ (F=4, m_F=0) π-transition DROR signal bandwidth on microwave field strength at different laser powers.

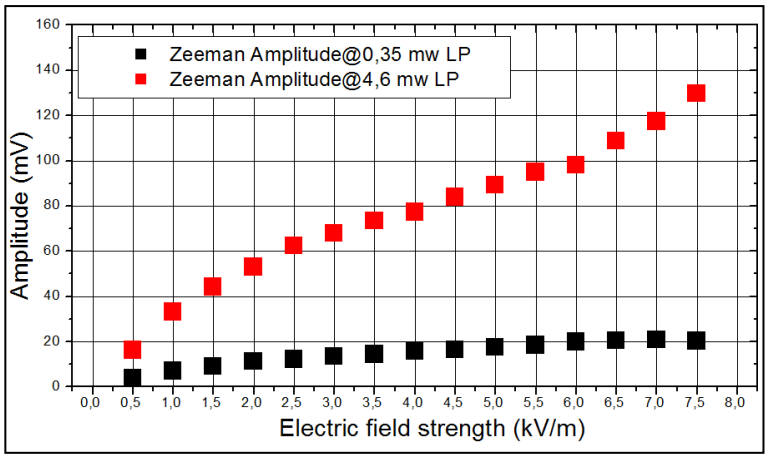

Figure 4.17: The dependency of the $6S_{1/2}$ (F =3, m_F=0) ↔ $6S_{1/2}$ (F =4, m_F=0) π-transition DROR signal amplitude on microwave field strength at different laser powers.

With the increase in the microwave field strength, the increase in the bandwidth (line width) of the Zeeman central component is expected to follow the

rule given in equation (4) below for the low laser powers [63].

$$\Delta\omega \sim a/2 + a/2\sqrt{1 + \frac{E^2}{b}} \quad (4)$$

Here; a center is the line width under minimum microwave field and at minimum laser power of the Zeeman signal. E is the electric field component of the microwave field. b variable is a constant depending on the other geometric parameters of the laser beam such as the laser diameter and the atom transition possibilities. According to this formula, the relation between the resonance bandwidth and the microwave field has the feature of being linear in the specified range.

In scope of the study, different laser and microwave power dependencies were studied to understand the behavior under high electromagnetic field, of the bandwidth and amplitude of $6S_{1/2}$ (F=3, m_F=0) ↔ $6S_{1/2}$ (F=4, m_F=0) π-transition as shown by the graphics in figure 4.16 and 4.17. This study was carried out in an approximately 1100 μT of static magnetic field, at different laser powers and microwave field levels. During the measurements the cesium tube was in the near field conditions of the horn antenna, and it was not possible to measure the field value in a clear way, and only theoretical calculation was possible to be made because the levels were highly exceeding the measurement range of the electric field probes.

During these measurements the laser powers were selected as 0,35 mW, 4,6 mW, respectively. The microwave field strengths were applied for each laser power at the values of 0,5 kV/m, 1 kV/m, 1,5 kV/m, 2 kV/m, 2,5 kV/m, 3 kV/m, 3,5 kV/m, 4 kV/m, 4,5 kV/m, 5 kV/m 5,5 kV/m, 6 kV/m, 6,5 kV/m, 7 kV/m, 7,5 kV/m, respectively. The bandwidth measurements were carried out at the point where the amplitude dropped to half, by using the "– width" detector of the oscilloscope. During the amplitude measurements the signal peak point was measured by using the "V amplitude" detector of the oscilloscope.

The measurement results in figure 4.16 and figure 4.17 can be interpreted as below: At fixed laser power, the increase in microwave field caused more atomic pumping between $6S_{1/2}$ (F=3) and $6S_{1/2}$ (F=4) energy levels. The laser locked between the $6S_{1/2}$ (F=4) ↔ $6P_{3/2}$ (F=4) levels interacted with higher number of atoms

and optic absorption was increased. Therefore the Zeeman signal amplitude at $6S_{1/2}$ (F=3, m_F=0) ↔ $6S_{1/2}$ (F=4, m_F=0) π-transition energy level increased also. The increase in the signal amplitude at measurements of the 0,35 mW is more linear based on low laser power levels, and nonlinearity tending of the graph was began after half of it. Owing to occurring saturation effect of the because of the larger optic pumping process at the high level laser powers at 4,6 mW, the nonlinearity tending of the graph much more began earlier. Because of the effect of the optic pumping caused by high laser powers, the number of atoms at $6S_{1/2}$ (F=4) level was reduced much more than the number of atoms transferred to this level by the microwave effect. Therefore the transitions occurring between the $6S_{1/2}$ (F=4) ↔ $6P_{3/2}$ (F=4) levels cannot be balanced. This situation caused non-linear increases at the amplitude and bandwidths of the resonances. Therefore the signal observed on the photodiode increased non-linearly depending on the laser power. In other words, the broadening in the resonances occurred at the high laser powers were not caused just because of the microwave field effect but also because of the laser beam. The laser power must be kept as low as possible to prevent any effect caused by the laser power during the resonance transition. This effect can be understood better by examining the figure 4.18 and figure 4.19.

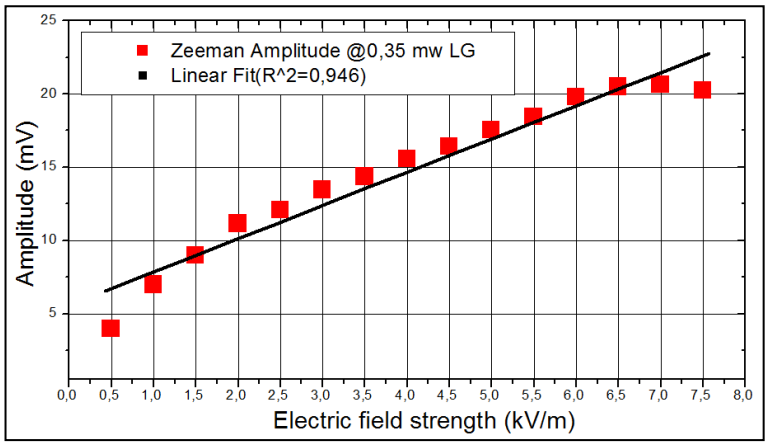

Figure 4.18**:** The dependency of $6S_{1/2}$ (F =3, m_F=0) ↔ $6S_{1/2}$ (F =4, m_F=0) π-transition DROR signal amplitude on microwave field strength at 0,35 mW fixed laser power.

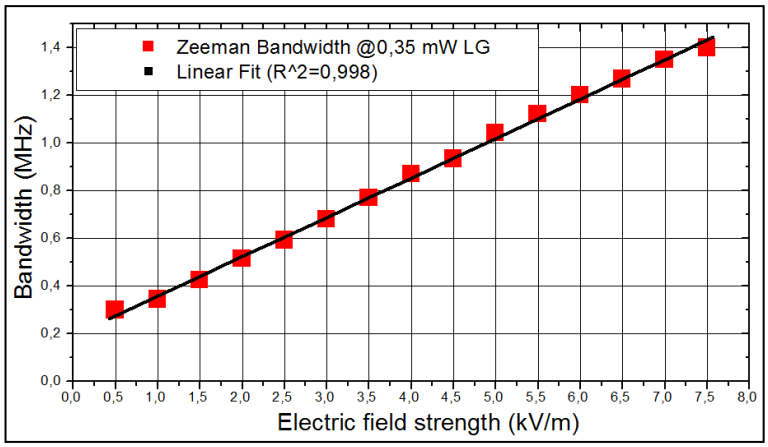

Figure 4.19: The dependency of $6S_{1/2}$ (F =3, m_F=0) ↔ $6S_{1/2}$ (F =4, m_F=0) π-transition DROR signal bandwidth on microwave field strength at 0,35 mW fixed laser power.

During these measurements obtained at 0,35 mW laser power, the effect of the laser power was minimized, and microwave field dynamic measurement range increased as linear. This linearity is more stably observed during bandwidth measurements (figure 4.19). When the microwave field strength was increased from 0.5 kV/m value to 7.5 kV/m value, the Zeeman DROR resonance line width broadened linearly from 0.3 MHz value to 1.4 MHz value as the result of the field broadening (power broadening) effect. As result of the linear fit approximation R^2 value for line width broadening measurement in figure 4.19 was obtained as 0,998. The R^2 value was found as 0,946 during the amplitude measurements in Figure 4.18. As seen in the amplitude measurements in Figure 4.18, the line width measurements show much more linear behavior when compared to the amplitude measurements.

The bandwidth measurements of DROR resonance Zeeman component (k=2 scope factor and 95% confidence range) were performed within 3 dB measurement uncertainty. 2 dB value is based on the applied microwave field uncertainty and the remaining 1 dB consists of uncertainty components such as standard deviation in amplitude measurements, oscilloscope frequency measurement uncertainty and the linearity of the photodiode in measuring the bandwidth.

The amplitude measurements of DROR resonance Zeeman component (k=2 scope factor and 95% confidence range) were performed under 4 dB of uncertainty. While the applied microwave field uncertainty is 2 dB as mentioned above, the uncertainty value from this part is 2 dB as the optic background noise, signal to noise

ratio, laser power changes and the photodiode saturation effects were more effective in the amplitude measurements of the resonance.

Consequently, the developed atomic sensor has the property of being used to sense the high level microwave fields by changing the dynamic range at suitable laser powers. But the saturation effects can be observed at very high laser powers, therefore the dynamic range to use the sensor needs to be well defined.

5. EXPERIMENTAL SETUPS, RESULTS AND DISCUSSIONS IN RC

Information will be provided in this third part of the thesis study about the setup used for atomic sensor measurements within the reverberation chamber, the methods of measurement and the measurement results. Afterwards the obtained experimental data is going to be discussed.

5.1 Experimental Setup in RC

First of all, unlike the anechoic chamber measurements, precise measurements were required at a single laser power, therefore the linearity measurements were carried out for the photodiode that showed the measurements were made at the point where at the range photodiode was linear. As the laser power that reaches the photodiode changes with the effects of microwave and various laser powers, the photodiode linearity characteristic measurement could directly affect the measurement results. Ensuring the photodiode linearity at the measurement range is very important. The measurements were obtained in two parts because of the filter configurations we had available, in order to obtain the same optic power values with the real measurements during the photodiode linearity measurements. That is why the photodiode linearity measurement results were shown in two individual images; figure 5.1 shows the measurement results between 0,1 uW and 0,5 uW and the figure 5.2 shows the results between 0,5 uW and 1 uW.

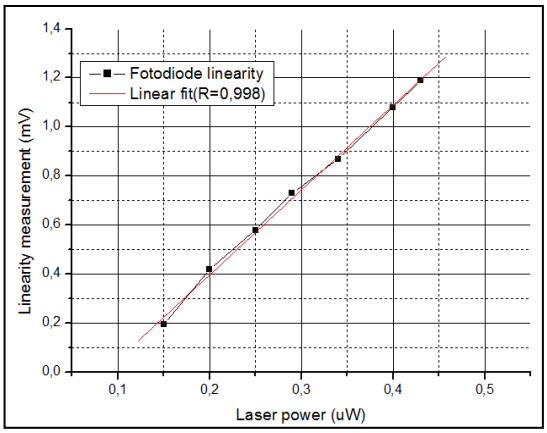

Figure 5.1: The result of the photodiode linearity between 0,1 uW-0,5 uW laser powers.

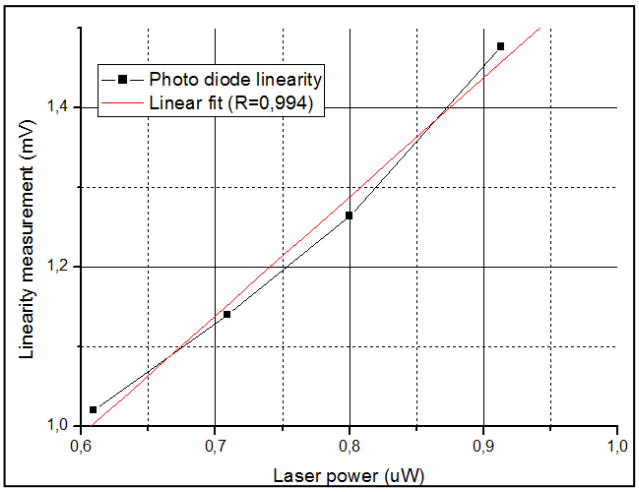

Figure 5.2: The result of the photodiode linearity between 0,5 uW-1 uW laser powers.

Thor labs S121C model optic sensor and PM100D model optic power meter and Agilent Technologies 34401A model multimeter were used at the measurements. The full schematic diagram of the relevant setup is shown in figure 5.3 and the measurement setup sample view is available in figure 5.4.

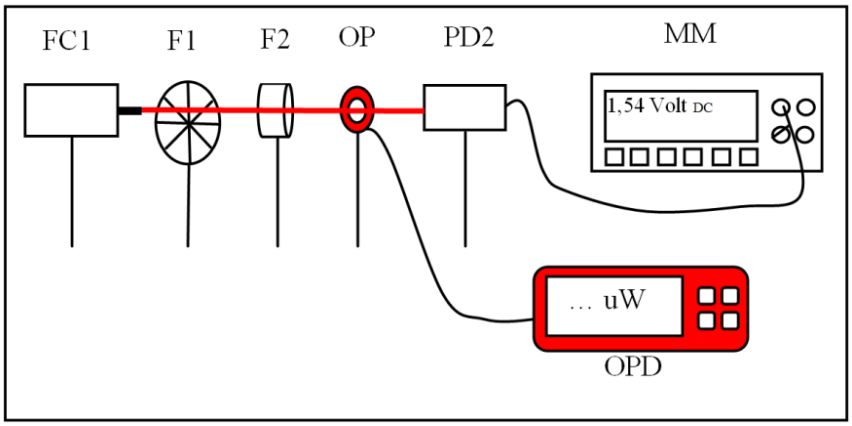

Figure 5.3: Photodiode linearity measurement setup.

In scope of the photodiode linearity measurements, firstly the maximum and minimum optic power values coming to the photodiode during the measurements were determined by including the increases caused by DROR effect. The laser power was adjusted to maximum at the input of Cs2 tube. Later, the maximum laser power was sent with the help of FC1 collimator to the adjustable F1 filter and from there, to the fixed F2 filter, and these optic power values were recorded with the help of OPD

optic power meter that was run at 852 nm at PD2 photodiode entrance. Later the OP optic power meter sensor was removed and the DC voltages that occurred at the photodiode exit that corresponded to the optic powers obtained during the same filter configurations were recorded by connecting a multimeter (MM). These measurements were repeated 10 times and an average value was obtained and the standard deviation value was calculated.

Figure 5.4: Photo from the photodiode linearity measurement setup.

The measurement setup of the atomic sensors within RC is almost the same as the one used in the anechoic chamber environment. But this stage the part within the anechoic chamber is within the reverberation chamber. The microwave field was generated with the horn antenna placed inside the reverberation chamber with the help of a wave guide. The first part of the optic measurement setup was established on the optic table outside the reverberation chamber. The block diagram of the measurement setup, on which the study was founded, is given in figure 5.5.

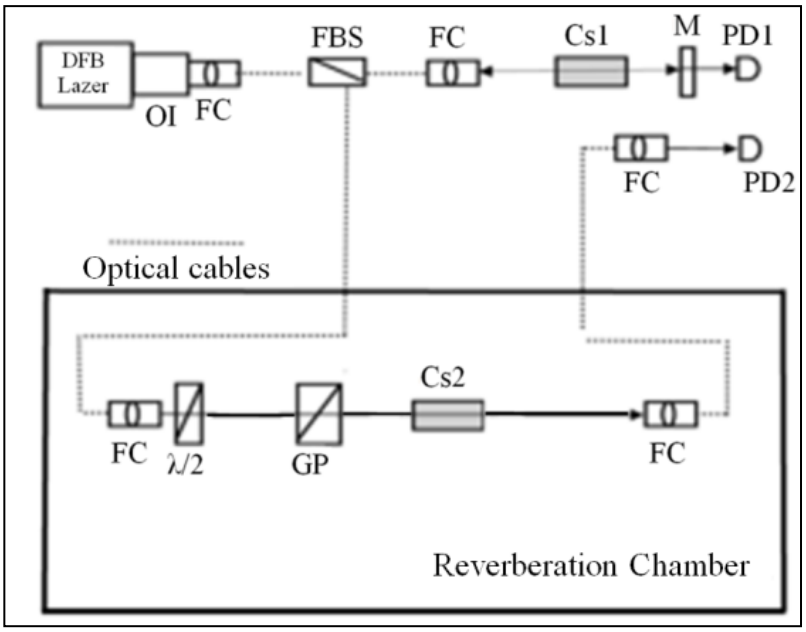

Figure 5.5: The block diagram of the experiment setup.

Although the optical measurement setup was exactly the same as the optical setup in the anechoic chamber measurements done before, there are some differences at the microwave field part. The part of the setup, where Cs2 test tube interacting with the microwave field was located, had been prepared within the reverberation chamber, in order to generate uniform and high level microwave field.

In scope of the optical measurement setup, as explained before for the anechoic chamber measurements, the microwave field generation was carried out after the process of locking the DFB laser frequency that scanned the $6S_{1/2}$ (F=4) and $6P_{3/2}$ (F=3, 4 and 5) transitions.

The microwave generation part of the setup included a microwave signal generator, a microwave power amplifier with 500 W output power and a standard-gain horn antenna. The power values transmitted in forward direction from RF sample port of the power amplifier was recorded to generate a controlled electric field by using horn antenna input, on Cs2 test cell.

The theoretical microwave field was not calculated for the measurements within the reverberation chamber, instead, the electric field probe was left within the chamber as the electric field level was below the level that could harm the probe, during the measurements. Therefore, by using an electric field probe, of which electric field value occurring on Cs2 tube was calibrated, we obtained the possibility of simultaneously measuring with an atomic sensor in real time. ETS-LINDGREN

company's Probe View LT software was used as a PC communication program to display the values measured by the electric field probe.

Accepting the electric field value measured by the electric field probe as a reference, the mixer (tuner) of the reverberation chamber was rotated in steps of 0.5º. The position of the tuner where the maximum electric field was measured, was recorded as 259,7º. This tuner position was kept fixed during the all measurements and no change was made within the chamber; the changes DROR resonances amplitudes of atomic sensor were recorded simultaneously with the values measured by the electric field probe.

Similar to the anechoic chamber measurements; DC power source, Helmholtz coils and a resistance of 0,5 Ω were used at the part the DC magnetic field was generated and where the measurement setup Zeeman splits were obtained. The voltages measure via 0,5 Ω resistance with the help of the multimeter were recorded at the magnetic field value required to generate the Zeeman components. The multimeter, DC power source, 0,5 Ohm etc. devices were kept outside the chamber to protect from the harmful effects of the high field generated within the reverberation chamber.

The laser polarization was kept linear during the measurements within the reverberation chamber. The measurements of the high level electromagnetic waves were performed in continuous wave mode by using this method.

The part of the optical measurement setup positioned on the wooden table within the reverberation chamber and the position of the horn antenna within the reverberation chamber are shown in figure 5.6. The sample view of the measurement setup within the reverberation chamber is shown in figure 5.7.

In the setup the cesium tube surrounded by DC Helmholtz coil, the horn antenna and the fiber heads that allow laser entries/exits were positioned within the reverberation chamber while the laser and microwave sources and all other relevant electronic devices were positioned outside the chamber.

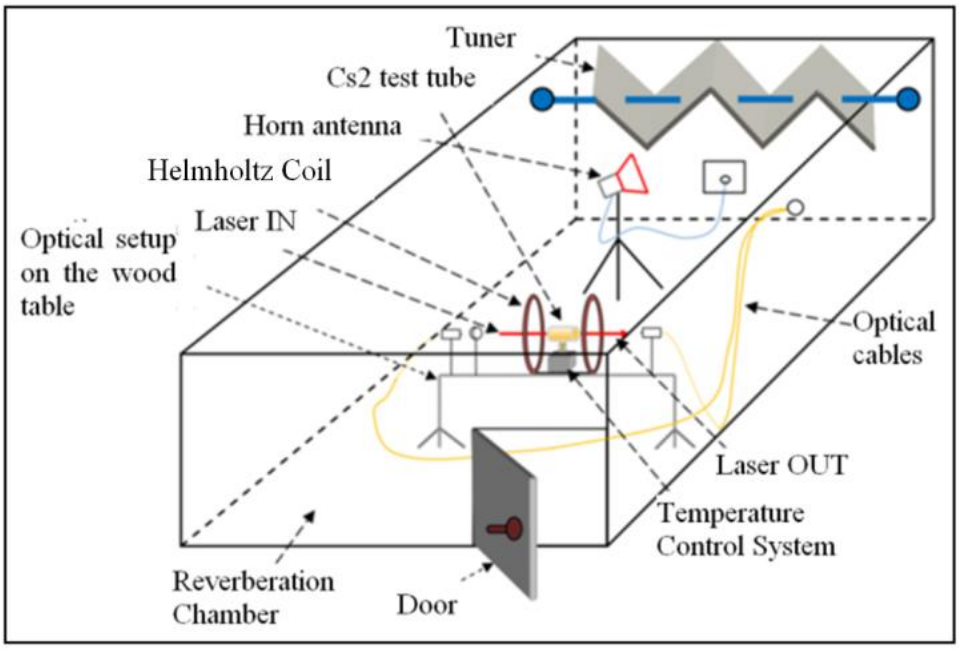

Figure 5.6: The measurement setup in the reverberation chamber.

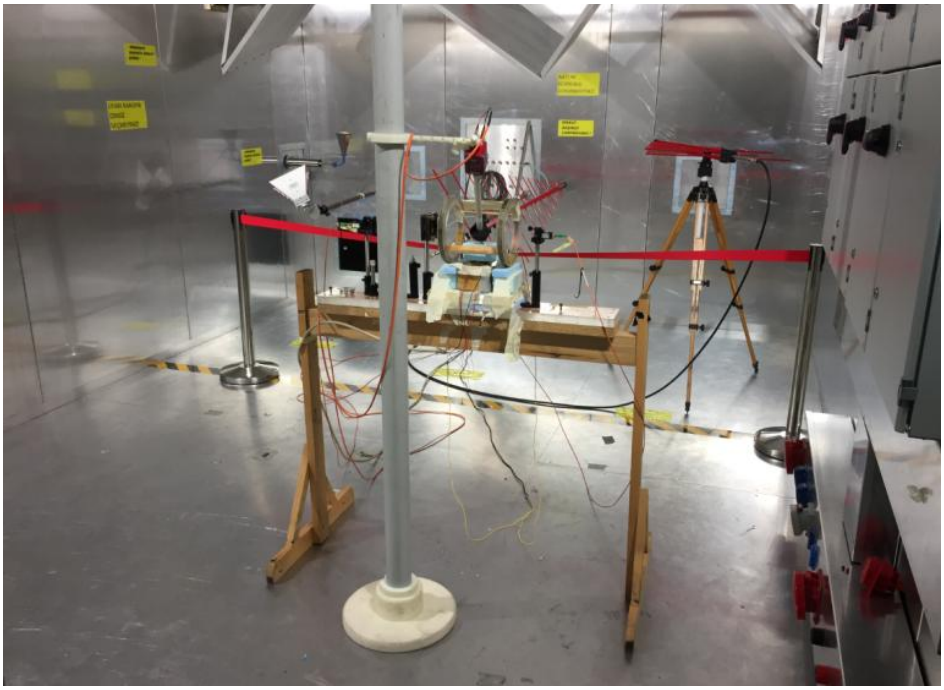

Figure 5.7: The sample view of the measurement setup in the reverberation chamber.

The position of the electric field probe at the location of Cs2 test tube during the reverberation chamber measurements is shown in photo figure 5.8 and the position of the horn antenna within the chamber is shown in photo figure 5.9.

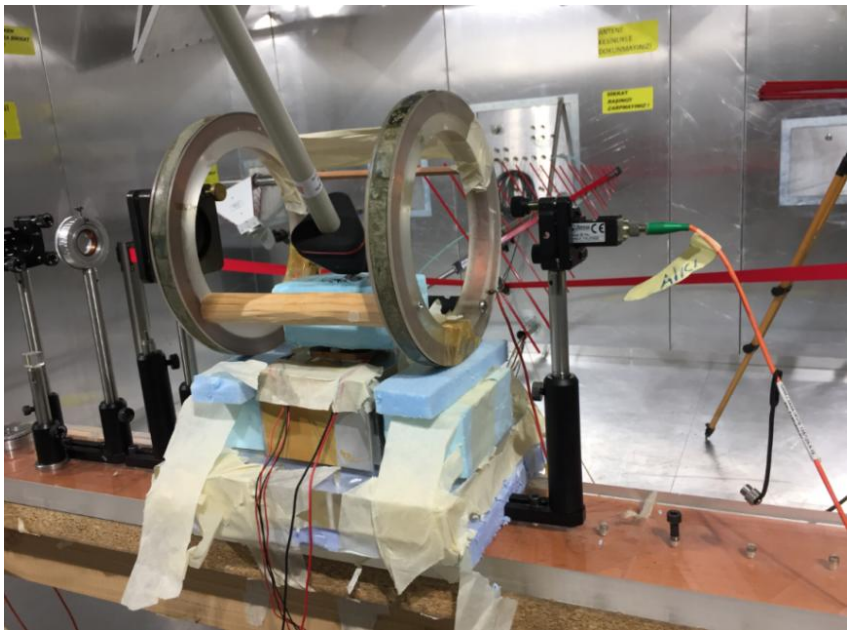

Figure 5.8: Electric field probe at the point of Cs2 test tube in Helmholtz coil.

Figure 5.9: Horn antenna location in RC.

5.2 Results and discussions in RC

The microwave field that can be generated within the reverberation chamber is only limited to the chamber dimensions and the microwave power amplifier maximum output power. With these chamber dimensions (4,9 (m) x 3,6 (m) x 3 (m)) and the 500 W power amplifier in the laboratory, maximum 500 V/m levels were achieved. These levels can be increased by using smaller chamber dimensions or by

using stronger special pulse amplifiers. Nevertheless, the value of the microwave field occurring within the reverberation chamber is a more efficient and real electric field value as it is a uniform electric field environment. The measurements within the reverberation chamber were carried out at 100 V/m, 200 V/m, 300 V/m, 400 V/m and 500 V/m levels. As the microwave field level is low, the measurements were made at maximum laser power 12,2 mW for maximum interaction. The bandwidth measurements were made at the point where the amplitude dropped to half by using the "- width" detector of the oscilloscope during the measurements while the amplitude measurements were made by using the "V amplitude" detector.

The tuner within the reverberation chamber was fixed at 259,7º during the measurements as it was the point where the electric field probe measured the maximum value. Similar to the anechoic chamber measurements, the laser polarization and DC magnetic field were adjusted in parallel with each other. As microwave field will carry out countless collision-reflection-overlap and damping processes within the reverberation chamber in various directions, it is not possible to talk about any microwave field direction.

The display of the DROR signal on the oscilloscope, for $6S_{1/2}$ (F=3) ↔ $6S_{1/2}$ (F=4) transition at 12,2 mW fixed laser power and fixed microwave field strength, is given in figure 5.10.

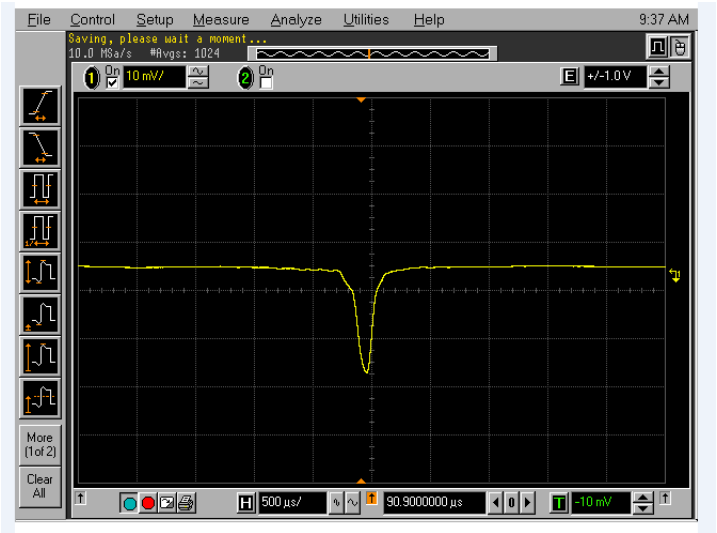

Figure 5.10: DROR resonance at 12,2 mW fixed laser power, for 300 V/m electric field strength.

The images of the DROR observed on the oscilloscope screen corresponding to the various microwave field levels at 12,2 mW fixed laser power are shown in figure 5.11.

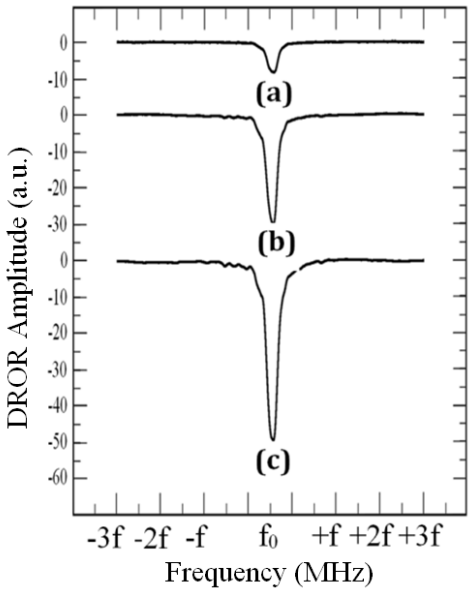

Figure 5.11: DROR signal amplitude changes of $6S_{1/2}$ (F=3) ↔ $6S_{1/2}$ (F=4) transition at different microwave field levels at 12,2 mW fixed laser power (in horizontal axis f_0≈9,192 GHz and f≈10 MHz), electric field levels a) 100 V/m, b) 300 V/m and c) 500 V/m.

After the DROR was observed on the oscilloscope screen in scope of these measurements, the Zeeman splits given in figure 5.12 were obtained under DC magnetic field.

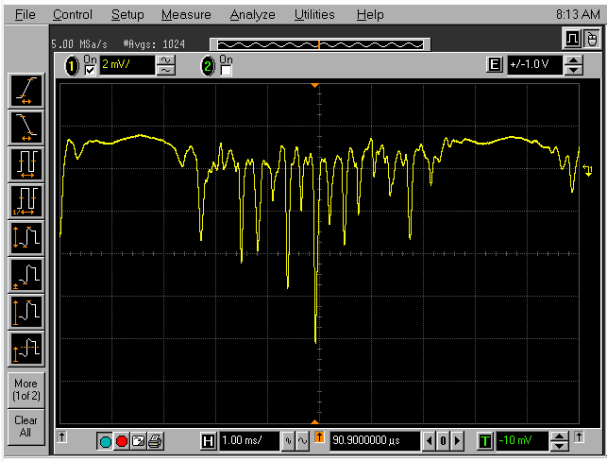

Figure 5.12: 15 Zeeman resonance of the DROR signal for $6S_{1/2}$ (F=3) ↔ $6S_{1/2}$ (F=4) transition at 12,2 mW fixed laser power and 500 V/m electric field strength.

The Zeeman resonances were asymmetrical when compared to the anechoic chamber measurements; the reason for this can be seen as the multiple direction microwave polarization which continuously changed and laser and atom interaction in the chamber.

The images of the 15 Zeeman resonances observed at various microwave field levels at fixed 12,2 mW laser power are given in figure 5.13.

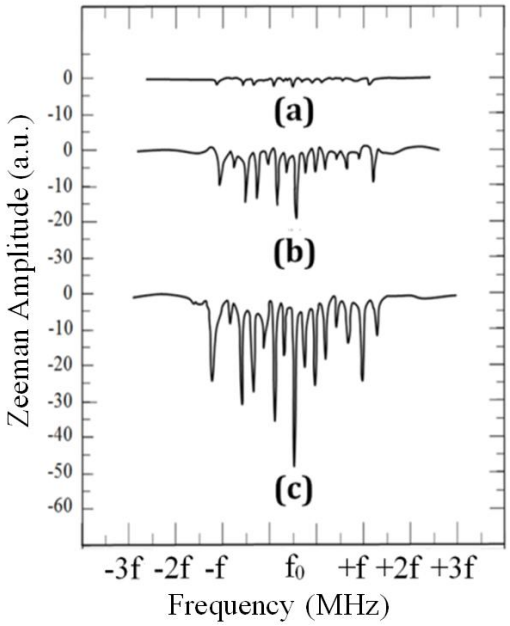

Figure 5.13: 15 Zeeman resonances observed at different microwave field levels at 12,2 mW fixed laser power (in horizontal axis $f_0 \approx 9{,}192$ GHz and $f \approx 10$ MHz) (a) 100 V/m, (c) 300 V/m, (d) 500 V/m.

After the Zeeman spectrum was observed on the oscilloscope display, the DC magnetic field value was increased up to approx. 1100 μT strength until only the central Zeeman component for $6S_{1/2}$ (F=3, m_F=0) ↔ $6S_{1/2}$ (F=4, m_F=0) π-transition remained. The oscilloscope screen image of the central Zeeman component for $6S_{1/2}$ (F=3, m_F=0) ↔ $6S_{1/2}$ (F=4, m_F=0) π-transition is given in figure 14.

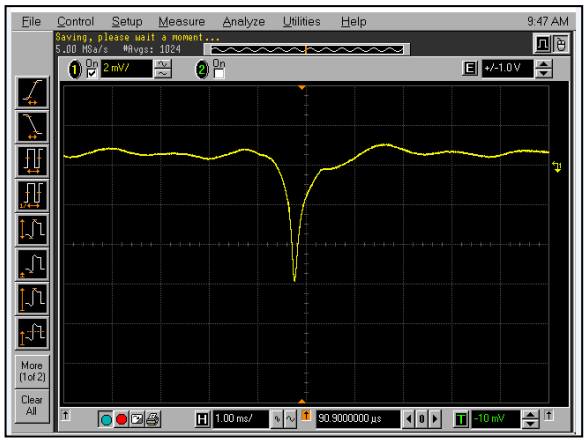

Figure 5.14: Central Zeeman component for $6S_{1/2}$ (F=3, m_F=0) ↔ $6S_{1/2}$ (F=4, m_F=0) π-transition at 12,2 mW fixed laser power, 300 V/m electric field strength.

The amplitude change of the central Zeeman component for $6S_{1/2}$ (F=3, m_F=0) ↔ $6S_{1/2}$ (F=4, m_F=0) -transition corresponding to the various microwave field strengths at fixed 12,2 mW laser power is given in figure 5.15.

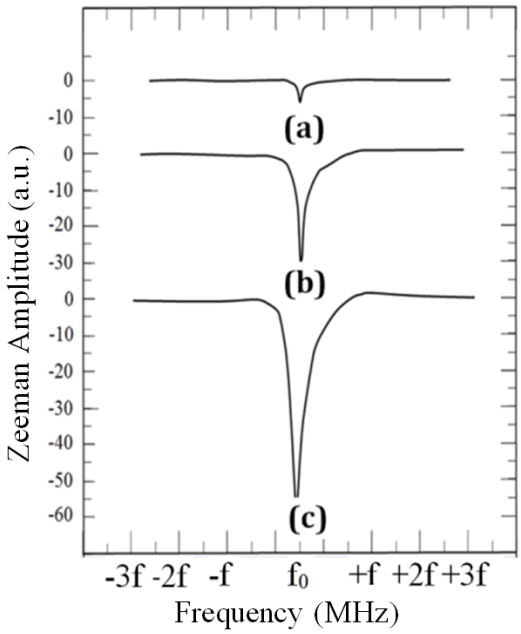

Figure 5.15. Central Zeeman component for $6S_{1/2}$ (F=3, m_F=0) ↔ $6S_{1/2}$ (F=4, m_F=0) π-transition at 12,2 mW fixed laser power and at different microwave field levels (in horizontal axis f_0≈9,192 GHz and f≈2 MHz), (a) 100 V/m electric field strength, (b) 300 V/m electric field strength, (c) 500 V/m electric field strength.

The graphic in the figure 5.16 shows the dependency of the DROR resonance amplitude during the $6S_{1/2}$ (F=3) ↔ $6S_{1/2}$ (F=4) transition on the microwave field

strength while the graphics that show the bandwidth and amplitude changes of the Zeeman resonance of $6S_{1/2}$ (F=3, m_F=0) ↔ $6S_{1/2}$ (F=4, m_F=0) π-transition are shown in figure 5.17 and 5.18, respectively.

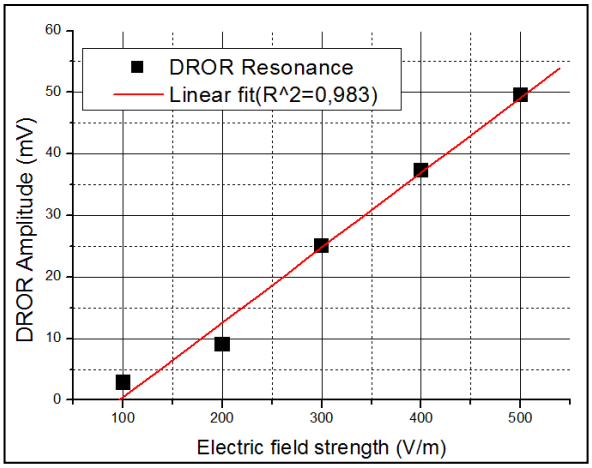

Figure 5.16: The dependency of DROR resonance amplitude on the microwave field strength at 12,2 mW fixed laser power during $6S_{1/2}$ (F=3) ↔ $6S_{1/2}$ (F=4) transition.

When the relation between the DROR resonance amplitude change shown in the graphic in figure 5.16 and the applied microwave field strength were linearly fitted, R^2 value was found as 0,983. When the microwave field strength was increased from 100 V/m value to 500 V/m value, DROR resonance amplitude broadened linearly from 2,8 mV value to 48,5 mV value as the result of the microwave effect.

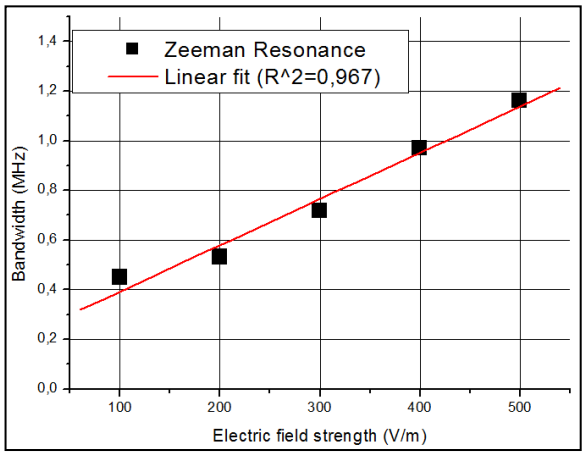

Figure 5.17: The dependency of Zeeman resonance bandwidth on the microwave field strength at 12,2 mW fixed laser power for $6S_{1/2}$ (F=3, m_F=0) ↔ $6S_{1/2}$ (F=4, m_F=0) π-transition.

When the microwave field strength was increased from 100 V/m value to 500 V/m value in figure 5.17, the bandwidth of the Zeeman signal linearly broadened from 0,45 MHz value to 1,16 MHz value as the result of the microwave effect during the DROR resonance $6S_{1/2}$ (F=3, m_F=0) ↔ $6S_{1/2}$ (F=4, m_F=0) π-transition.

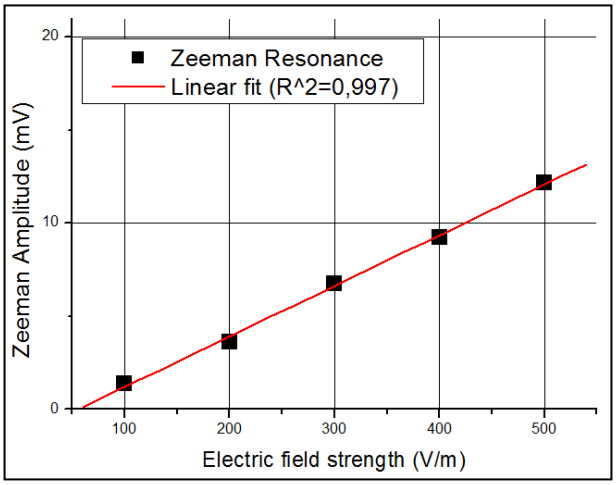

Figure 5.18: The dependency of Zeeman resonance amplitude on the microwave field strength at 12,2 mW fixed laser power for $6S_{1/2}$ (F=3, m_F=0) ↔ $6S_{1/2}$ (F=4, m_F=0) π-transition.

In figure 5.18, when the microwave field strength was increased from 100 V/m value to 500 V/m value the amplitude of the Zeeman signal corresponding to $6S_{1/2}$ (F=3, m_F=0) ↔ $6S_{1/2}$ (F=4, $_F$=0) π-transition of the DROR resonance linearly broadened from 1,39 mV value to 12,17 mV value as the result of the microwave effect.

When the figure 5.17 and figure 5.18 are interpreted together, it is seen the bandwidth linearly increases with the increase in the central Zeeman component amplitude at $6S_{1/2}$ (F=3, m_F=0) ↔ $6S_{1/2}$ (F=4, m_F=0) π-transition with the increasing microwave field strength. When the dependency of the central Zeeman component during $6S_{1/2}$ (F=3, m_F=0) ↔ $6S_{1/2}$ (F=4, m_F=0) π-transition on the microwave field strength given in 5.17 was linearly fitted, the R^2 value was found as 0,967; when the dependency of the amplitude of the Zeeman resonance in figure 5.18 on the microwave field was linearly fitted, the R^2 value was found as 0,997. The R^2 values found for the linear fit shows that the Zeeman bandwidth and amplitude changes measured in scope of the study are between 100 V/m-500 V/m microwave field

levels. But as mentioned at the beginning of the thesis, the optical background noise, signal to noise ratio and photodiode saturation etc. some disruptive factors exist during the amplitude and bandwidth measurements of the resonance. Although the mentioned negative factors may directly affect the amplitude measurements of the resonance, they will be felt less as the resonance bandwidth measurements were carried out at the horizontal axis and dependent on the frequency.

Amplitude measurements of the DROR resonance (k=2 scope factor and 95% confidence range) were performed with 3,5 dB measurement uncertainty in total. Here, the 2,5 dB value is the uncertainty of applied microwave field while the 1 dB value is the uncertainty of contribution of the environmental factors such as the optical background noise, signal to noise ratio, laser power changes and photodiode saturation effects.

The bandwidth measurements of DROR signal Zeeman component (k=2 scope factor and 95% confidence range) were carried out within 4 dB measurement uncertainty. Here, 3 dB value is based on the applied microwave field uncertainty and the remaining 1 dB consists of uncertainty components such as standard deviation in amplitude measurements, oscilloscope frequency measurement uncertainty and the linearity of the photodiode in measuring the bandwidth.

The amplitude measurements of DROR signal Zeeman component (k=2 scope factor and 95% confidence range) were carried out under 4,5 dB of uncertainty. While the generated microwave field uncertainty here was 3 dB, the uncertainty value from this part was 1,5 dB as the optic background noise, signal to noise ratio, laser power changes and the photodiode saturation effects were more effective in the amplitude measurements of the resonance.

6. CONCLUSION

In this thesis study we worked on an electromagnetic field measurement system based on laser-atom interaction. Atomic sensors have the capacity for measuring without harmonic, has small size and dielectric structure in addition to having many superior aspects and the potential to become an alternative at measurement high level microwave fields generated in reverberation chambers. Today, the classical electromagnetic measurement systems are not enough to measure high level microwave fields generated in reverberation chambers.

For this purpose, firstly the differences between the analysis results of the reverberation chamber calibration and test measurements defined by various standards were explained. Although the calibrations were basically the same, the importance of the standards selected for the test measurement analyses was explained.

In the second part the maximum field levels measurable with this atomic sensor in scope of the devices available in the laboratory were reached and dynamic operation ranges of the atomic sensor at these levels were investigated at different laser powers. The resonances expected to be seen in compliance with the theory were observed and measurements were made with these resonances. The relation between the applied electromagnetic field and the resonances obtained from the atomic transitions was investigated and the relation was found to be linear. When the results obtained in the second part was evaluated, it was found the atomic sensor dynamic measurement range can be changed by using the laser power. When the dynamic range was suitable adjusted, it was determined the linear relation between the high microwave fields and Zeeman component amplitude and bandwidths was preserved. As emphasized at the beginning of the study, it was more advantageous to perform the microwave field measurements based on the bandwidth of the Zeeman component of DROR resonance. Consequently it was determined the band width measurements showed more linear increase when compared to the amplitude measurements, as anticipated.

Lastly, in the third part, an atomic sensor was placed within the reverberation chamber for the first time in the literature, which was a completely uniform and direction-independent electromagnetic field environment and its behaviors were researched at 9,192 GHz frequency under high level microwave field. For this

purpose the DROR resonances and Zeeman components obtained from Cs atom energy transitions in the uniform and high level electromagnetic field environment generated within the reverberation chamber were obtained. The amplitude measurements of DROR resonance, as well as the bandwidth and amplitude measurements of the central Zeeman resonance among such resonances of $6S_{1/2}$ (F=3, m_F=0) ↔ $6S_{1/2}$ (F=4, m_F=0) π-transition were carried out at maximum microwave field levels that was possible to achieve in scope of the study. The relation between these resonances obtained from the atomic transitions and the microwave field strength generated within the reverberation chamber was studied. The bandwidth and amplitude measurements of Zeeman resonance and the DROR resonance amplitude measurements of the atomic sensor were performed at the maximum field levels. As the result of this experiments, it was concluded that when we calibrate the atomic sensors under a known microwave field within a fully anechoic chamber, which by using the DROR amplitude resonances or Zeeman bandwidth and amplitude resonances could be possible to measure the microwave field strength at high levels within the reverberation chambers with the help of the reference values.

Consequently it can be said that a measurement method has been developed in this study. This method has the capacity to measure the high level microwave field value occurring within the reverberation chamber in real time. When the Zeeman bandwidth measurements of the atomic sensor system are suitably arranged the atomic sensor, can stay within the chamber during the test measurements performed at high levels and during the calibration of the reverberation chambers. Moreover, the method developed in this study can be beneficial in terms of the application measurements and in sensing the high level electromagnetic fields by using the atomic sensors.

REFERENCES

[1] Mendes H. A., (1968) “A new approach to electromagnetic field-strength measurements in shielded enclosures”, Wescon, Los Angeles.

[2] Corona P., (1980), “Electromagnetic reverberating enclosures: behavior and applications”, Al ta Frequenza, 49, 154-158.

[3] Corona P., Latmiral G., (1976), “Evaluation and use of the reverberating chamber of the Istituto Universitario”, Naval e, First National Meeting of Applied Electromagnetism, Italy.

[4] Corona P., Latmiral G., (1978), “Thermodynamic approach to the study of a variable geometry electromagnetic reverberating room (in Italian)”, Instituto Universitario Naval e, Naples, Italy.

[5] Corona P., Latmiral G., Paolini E., Piccioli L., (1976), “Use of a reverberating enclosure for measurements of radiated power in the microwave range”, IEEE Trans. EMC-18, 54-59.

[6] Corona P., Latmiral G, Paolini E, Piccioli L., (1977), “Performance of a reverberating enclosure for power measurements in the microwave range”, Proc. 2nd Symposium and Technical Exhibition on EMC, 419- 423, Montreux.

[7] Corona P., De Bonitatibus A., Ferrara G., Paolini E., (1979), “Electromagnetic enclosures behavior comparison data analysis”, Proc. 3rd Symposium and Technical Exhibition on EMC, 231-236, Rotterdam.

[8] Corona P., Latmiral G., Paolini E., (1980) “Performance and analysis of a reverberating enclosure with variable geometry”, IEEE Trans. EMC-22, 2- 5.

[9] Liu B.H., Chang D.C., Ma M.T., (1983), “Eigenmodes and the composite quality factor of a reverberating chamber”, Nat. Bur. Stand. Technical Note 1066, U.S.

[10] Hatfield M. O., Slocum M. B., Godfrey E. A., Freyer G. J., (1998), "Investigations to extend the lower frequency limit of reverberation chambers”, IEEE International Symposium on Electromagnetic Compatibility, 1, 20-23.

[11] Ladbury J., Koepke G., Camell D., (1999), “Evaluation of the NASA Langley Research Center Mode-Stirred Chamber Facility”, US Dept. Commerce, Boulder, CO, NIST Tech. Note 1508.

[12] Holloway C. L., Hill D. A., Ladbury J. M., Wilson P., Koepke G., Coder J., (2006), “On the use of reverberation chambers to simulate a controllable Rician radio environment for the testing of wireless devices”, IEEE Trans. Antennas Propag. Special Issue on Wireless Communications, 54, 11, 3167–3177.

[13] Ladbury J. M., Hill D. A., (2010), “An improved model for antennas in reverberation chambers”, IEEE Int. Symp. on Electromagnetic Compatibility, 25–30, 663–667.

[14] Holloway C. L., Shah H., Pirkl R. J., Remley K. A., Hill D. A., Ladbury J., (2012), “Early-time behavior in reverberation chambers and its effect on the relationships between coherence bandwidth, chamber decay time, rms delay spread, and the chamber build-up time”, IEEE Trans. EMC.

[15] Remley K. A., Dortmans J., Weldon C., Horansky R. D., Meurs T. B., Wang C.M., Williams D. F., Holloway C. L., Wilson P. F., (2016), "Configuring and verifying reverberation chambers for testing cellular wirelss devices", IEEE Trans. Electromagn. Compat., 58, 3, 661-672.

[16] Senic D., Williams D. F., Remley K. A., Wang C.M., Holloway C. L., Yang Z., Warnick K. F., (2017), "Improved antenna efficiency measurement uncertainty in a reverberation chamber at millimeter-wave frequencies", IEEE Trans. Antennas Propag., 65, 8, 4209-4219.

[17] IEC 61000-4-21, “Testing and measurement techniques-Reverberation chamber test methods”.

[18] RTCA DO-160F, “Environmental Conditions and Test Procedures for Airborne Equipment”.

[19] RTCA DO-160G, “Environmental Conditions and Test Procedures for Airborne Equipment”.

[20] MIL-STD-461F, “Requirements for the Control of Electromagnetic Interference Characteristics of Subsystems and Equipment”.

[21] Çakır S., Aslan Ç., Leferink F., (2017), “Comparison of Test Standards for Immunity Testing in Reverberation Chambers”, Asia-Pacific International Symposium on Electromagnetic Compatibility (APEMC), Seoul, Korea.

[22] Kanda M., Driver L. D., (1987), “An isotropic electric-field probe with tapered resistive dipoles for broad-band use 100 kHz to 18 GHz”, IEEE Trans. Microw. Theory Tech., 35, 124-130.

[23] Alexander M. J., Salter M. J., Loader B. G., Knight D. A., (2002), “Broadband calculable dipole reference antennas”, IEEE Trans. Electromagn. Compat., 44, 45-58.

[24] Kanda M., Ries F. X., (1981), “A broad-band isotropic real-time electric-field sensor (BIERS) using resistively loaded dipoles”, IEEE Trans. Electromagn. Compat., 23, 122-132.

[25] Alexander M. J., Salter M. J., Gentle D. G., Knight D. A., Loader B. G., Holland K. P., (2004), “Calibration and use of antennas, focusing on EMC applications”, Meas. Good Practice Guide No 7, Nat. Phys. Lab., Teddington, U.K.

[26] Berger H. S., Kumara V., Matloubi M., (1988), “Consideration in the design of a broadband E-field sensing system”, IEEE Symp. Electromagn. Compat., Seattle, ABD.

[27] Web 1, (2017), https://www.bipm.org/en/measurement-units/rev-si/.

[28] Web 2, (2017), https://www.bipm.org/cc/CCEM/Allowed/30/CCEM-17-Report-NIST.pdf.

[29] Rabi I. I., (1937), “Space quantization in a gyrating magnetic field”, Phys. Rev., 51, 652-654.

[30] Kastler A., (1950), “Production et detection optique d'une inegalite de population”, J. Phys. Radium, 11, 255-265.

[31] Dehmelt H. G., (1957), “Modulation of a light beam by precessing absorbing atoms”, Phys. Rev., 105, 1924-1925.

[32] Bell W. E., Bloom A., (1957), “Optical detection of magnetic resonance in alkali metal vapor”, Phys. Rev., 107, 1559-1565.

[33] Ali A. W., Griem H. R., (1966), “Theory of Resonance Broadening of Spectral Lines by Atom-Atom Impacts” Phys. Rev.140, A1044 – Published 15 November 1965; Erratum Phys. Rev., 144, 366.

[34] Aleksandrov E. B., Mamyrin A. B., Naumov A. P., (1977), “Hfs-magnetometer for absolute measurement of magnetic induction of weak magnetic-fields”, Meas. Tech., 20, 1048-1051.

[35] Happer W., (1972), “Optical pumping” Rev. Mod. Phys., 44, 169–249.

[36] Osterwalder A., Merkt F., (1999), “Using high Rydberg states as electric field sensors”, Phys. Rev. Lett., 82, 1831-1834.

[37] Donley E. A., Crowley T. P., Heavner T. P., Riddle B. F., (2003), "Quantum-based microwave power measurement performed with a miniature atomic fountain", Proc. IEEE Int. Frequency Control Symp., 135-137.

[38] Savukov I. M. S. S., Romalis M. V., Sauer K. L., (2005), “Tunable atomic magnetometer for detection of radio-frequency magnetic fields”, Phys. Rev. Lett., 95, 063004.

[39] Crowley T. P., Donley E. A., Heavner T. P., (2004), “Quantum-based microwave power measurements: Proof-of-concept experiment”, Rev. Sci. Instrum., 75, 2575-2580.

[40] Paulusse D. C., Rowell N. L., Michaud A., (2005), “Accuracy of an atomic microwave power standard”, IEEE Trans. Instrum. Meas., 54, 2, 692-695.

[41] Çetintaş M., Hamid R., Şen O., Çakır S., (2009), "Traceable field strength measurements based on laser spectroscopy techniques", TP-2 20th Int. Zurich Symp. Electromagn. Compat., Zurich, Switzerland.

[42] Çetintaş M., Hamid R., Şen O., Çakır S., (2010), "Characterization of a far-field microwave magnetic field strength sensor based on double radiooptical resonance," IEEE Trans. Electromagn. Compat., 52, 1, 21–31.

[43] Çetintaş M., Çakır S., Hamid R., Şen O., (2012), "Toward absolute measurements of far-field microwave magnetic field by atomic sensor based on double radiooptical resonance", IEEE Trans. on Electromagnetic Compat., 54, 1, 225-227.

[44] Çakır S., Hamid R., Çetintaş M., Çakır G., Şen O., (2012), "Sensing of RF Magnetic Fields Using Zeeman Splitting of Double Radiooptical Resonance and a New Approach to Helmholtz Coil Calibrations", Sensors Journal IEEE, 12, 7, 2465-2473.

[45] Vanier J., Godone A., Levi F., (1998), "Coherent population trapping in cesium: Dark lines and coherent microwave emission", Phys. Rev. A, 58, 3, 2345–2358.

[46] Nagel A., Graf L., Naumov A., Mariotti E., Biancalana V., Meschede D., Wynands R., (1998), "Experimental realization of coherent dark-state magnetometers", Europhys. Lett., 44, 1, 31–36.

[47] Wynands R., Nagel A., Brandt S., Meschede D., Weis A., (1998), "Selection rules and line strengths of Zeeman-split dark resonances", Phys. Rev. A, 58, 1, 196–203.

[48] Ripka P., Janosek M., (2010), "Advances in magnetic field sensors," IEEE Sensors J., 10, 6, 1108–1116.

[49] Lenz J., Edelstein A. S., (2006), "Magnetic sensors and their applications", IEEE Sensors J., 6, 3, 631–649.

[50] Kitching J., Knappe S., Donley E. A., (2011), "Atomic sensors-a review", IEEE Sensors J., 11, 9, 1749–1758.

[51] Zibrov A. S., Zhukov A. A., Yakovlev V. P., Velichansky V. L., (2006), "Shape of the signal of double radio-optical resonance in 85Rb atomic vapors in strong fields" JETP Lett., 83, 4, 136–140.

[52] Litvinov A., Kazakov G., Matisov B., Mazets I., (2008), "Double radio-optical resonance in 87Rb atomic vapour in a finite-size buferless cell", J. Phys. B: At. Mol. Opt. Phys., 41, 125401-1–8.

[53] Paulusse D., Rowell N., Michaud A., (2002), "Realization of a atomic microwave power standard", Proc. Conf. Precision Electromagn. Meas., Ottawa, Canada, 194–195.

[54] Holloway C. L., Gordon J. A., Simons M. T., Fan H., Kumar S., Shaffer J. P., Anderson D. A., Schwarzkopf A., Miller S. A., Thaicharoen N., Raithel G., (2015), "Atom-based RF electric field measurements: An initial investigation of the measurement uncertainties", Electromagnetic Compatibility IEEE International Symposium, 467-472.

[55] Fan H., Kumar S., Sedlacek J., Kübler H., Karimkashi S., Shaffer J. P, (2015), "Atom based RF electric field sensing", Journal of Physics B: Atomic, Molecular and Optical Physics, 48, 202001.

[56] Holloway C. L., Gordon J.A., Jefferts S., Schwarzkopf A., Anderson D. A., Miller S. A., Thaicharoen N., Raithel G., (2014), "Broadband Rydberg Atom-Based Electric-Field Probe for SI-Traceable Self-Calibrated Measurements", Antennas and Propagation IEEE Transactions, 62, 12, 6169-6182.

[57] Song Z., Feng Z., Liu X., Li D., Zhang H., Liu J., Zhang L., (2017), "Quantum-Based Determination of Antenna Finite Range Gain by Using Rydberg Atoms", Antennas and Wireless Propagation Letters IEEE, 16, 1589-1592.

[58] Song Z., Zhang W., Liu X., Zou H., Zhang J., Jiang Z., Qu J., (2018), "Quantum-Based Amplitude Modulation Radio Receiver Using Rydberg Atoms", Globecom Workshops IEEE, 1-6.

[59] Leo R., Primiani V. M., (2006), "Radiated immunity tests: reverberation chamber versus anechoic chamber results" IEEE Transactions on Instrumentation and Measurement, 55, 4, 1169-1174.

[60] Arnaut L. R., Krauthauser H. G., Hoijer M., (2007), "Comparison of Different Definitions of Field Strength Used in Reverberation Chamber Standards", Proc. of IEEE International Symposium on Electromagnetic Compatibility, EMC 2007.

[61] Fanning C.W., (2006), "Achieving correlation of radiated rf immunity testing performed in an absorber lined shielded enclosure and a mode tuned reverberation chamber", Proc. of IEEE International Symposium on Electromagnetic Compatibility, EMC 2006.

[62] Steck D. A., (2010), "Cesium D Line Data", revision 2.1.4

[63] Demtröder W., (1996), "Laser Spectroscopy", 2nd ed., Springer-Verlag, New York.

[64] Gamidov R.G., Taşkın İ., Çetintaş M., Sautenkov V., (1996), "Unmodulated External-Cavity Diode Laser Stabilized on Cesium D_2 Line", IEE Proc. Science, Measurement and Technology, 143, 4, 263-264.

BIOGRAPHY

Çağlar ASLAN was born in 1989. He completed his undergraduate education by graduating from Erciyes University / Department of Physics in 2012. He has begun to work as a researcher in the Electromagnetic Laboratory of TÜBİTAK UME (National Metrology Institute) in 2014. He has begun his graduate study at the 2016 at Gebze Technical University / Department of Physics, in Metrology Master Program. He is currently working at TÜBİTAK UME Electromagnetic Laboratory. He is married and he has two unique and wonderful sons named Asrın and Mirali.